NAS5-30756

EARTH OBSERVING SCANNING POLARIMETER (EOSP)

PHASE-B FINAL REPORT

PREPARED FOR
NATIONAL AERONAUTICS AND SPACE ADMINISTRATION
GODDARD SPACE FLIGHT CENTER
Greenbelt Road, Greenbelt, MD 20771
and
GODDARD SPACE FLIGHT CENTER
INSTITUTE FOR SPACE STUDIES
2880 Broadway, New York, NY 10025

CONTRACT NO. NAS5-30756
CDRL SEQUENCE NUMBER 3
DM LB87-0016
SBRC REF. 90-1056
DECEMBER 1990

SANTA BARBARA RESEARCH CENTER

A Subsidiary of Hughes Aircraft Company

75 COROMAR DRIVE, GOLETA, CALIFORNIA

EARTH OBSERVING SCANNING POLARIMETER (EOSP)

PHASE-B FINAL REPORT

Prepared For

NATIONAL AERONAUTICS AND SPACE ADMINISTRATION
GODDARD SPACE FLIGHT CENTER
Greenbelt Road, Greenbelt, MD 20771

and

GODDARD SPACE FLIGHT CENTER
INSTITUTE FOR SPACE STUDIES
2880 Broadway, New York, NY 10025

Contract No. NAS5-30756

CDRL Sequence Number 3

DM LB87-0016

SBRC Reference No. 90-1056

December 1990

CONTENTS

ILLUSTRATIONS

TABLES

ABSTRACT

This report summarized evaluations performed during a Phase B study directed towards defining an optimal design for the Earth Observing Scanning Polarimeter (EOSP) instrument. An overview of the experiment approach is included which provides a summary of the scientific objectives, the background of the measurement approach, and the measurement method. In the instrumentation section, details of the design are discussed starting with the key instrument features required to accomplish the scientific objectives and a system characterization in terms of the Stokes vector/Mueller matrix formalism. This is followed by a detailing of the instrument design concept, the design of the individual elements of the system, the predicted performance, and a summary of appropriate instrument testing and calibration. The selected design makes use of key features of predecessor polarimeters and is fully compatible with the Earth Observing System spacecraft requirements.

Section 1
EXPERIMENT APPROACH

1.1 SCIENTIFIC OBJECTIVES

The measurement objectives of the Earth Observing Scanning Polarimeter (EOSP) are to observe the global, long-term distributions of radiance and linear polarization degree for twelve spectral bands in the visible and near infrared in order to produce a global climatology of: (1) cloud properties including optical thickness, particle size, liquid/ice phase, and cloudtop pressure; and (2) optical thickness of stratospheric and tropospheric aerosols. In addition, these measurements can be used to: (1) provide atmospheric correction information for ocean and land observations by other Earth Observing System (Eos) instruments; (2) investigate variations in aerosol sizes and optical properties indicative of composition changes, together with associated variations in cloud optical properties; and (3) investigate relation of observed land surface characteristics to vegetation and soil properties.

One of the key science tasks for the Eos Mission is to characterize the large-scale and low-frequency variability of clouds and to determine the effect of clouds on the net incoming solar radiation and the net outgoing long-wave radiation. Since cloud feedbacks represent the principal uncertainty in understanding climate sensitivity (e.g., Hansen et al., in Climate Processes and Climate Sensitivity, Geophys. Monograph 29, AGU, 130, 1984), extension and improvement of existing cloud climatology efforts through the systematic approach of Eos is crucial for addressing this problem. Global maps of spectral radiance and linear polarization degree obtained by EOSP will permit the compilation of a systematic climatology of critical cloud parameters essential for quantifying the radiative role of clouds. Specifically, the EOSP observations will be applied to the routine determination of cloud optical thickness, particle size and phase at the top of the cloud, and the pressure level of the cloudtop.

Aerosols represent another important atmospheric component that has an important role in radiative processes. In addition, aerosols act as condensation nuclei and thus affect cloud formation and the optical thickness of clouds (Coakley et al., Science 237, 1020, 1987). Of course, there is great diversity in type, source, and distribution of aerosols ranging from windblown dust, sea spray residue, and smog to stratospheric aerosols of volcanic origin due largely to sulfur dioxide emissions converted to sulfuric acid droplets and particles composed of sulfate salts. The EOSP polarization measurements will constitute a very sensitive detector of the presence of aerosols. These measurements will allow determination of the global distribution and optical thickness of the stratospheric aerosols and provide the same information for tropospheric aerosols for cloud-free conditions.

Virtually all satellite remote sensing of land and oceans at visible and near-infrared wavelengths requires an atmospheric correction to remove effects of molecular and aerosol scattering. Although various empirical approaches, typically involving ratioing of normalized radiances in different spectral bands, have been employed for making atmospheric correction estimates, the optimum approach is based on corrections computed using radiative transfer models which include detailed specification of the aerosol optical properties. The determination of aerosol optical properties from the EOSP polarimetry will thus allow the latter approach to be applied when accurate atmospheric corrections are vital. Moreover, the establishment of an aerosol climatology is the key to developing atmospheric correction techniques which have the advantage of radiative transfer models but reduce the computational cost for specific applications through the creation of a large set of pre-computed standard cases.

1.2 BACKGROUND FOR MEASUREMENT APPROACH

With but very few exceptions, remote sensing of sunlight reflected and scattered from surfaces and atmospheres is restricted to measurements that utilize only the radiance (or intensity). The linear polarization degree and the direction of polarization, which contains significant information about the nature of the surface or atmospheric scatterers, is rarely a measurement objective. There are two principal reasons for this. First, much more care is required in instrument design to make sufficiently accurate polarization measurements compared to radiance observations only. Emphasis is often placed on obtaining improved spectral coverage rather than investing instrument resources on polarimetry. The second factor which may have limited the interest in polarimetry as a remote sensing tool was the relative complexity of the modeling techniques necessary for interpreting such observations. An effective method for handling multiple scattering including polarization was developed and described some time ago (Hansen, J. Atmos. Sci. 28, 120, 1971), but only recently the rapid increase in speed and memory of the typical mainframe computer has brought detailed polarization analysis within reach of relatively modest computational resources.

The power of polarimetry as a remote sensing tool has been convincingly demonstrated by Hansen and colleagues (Hansen and Arking, Science 171, 669, 1971; Hansen and Hovenier, J. Atmos. Sci. 31, 1137, 1974). Through the analysis of ground-based polarization observations of Venus, they were able to establish that the thick clouds which completely shroud the planet consist of particles that are spherical (and therefore in liquid phase). The Venus cloud particles were found to have a narrow size distribution with an effective particle radius of 1.05 μm; the refractive index of the particles was 1.43 at 990 nm, 1.44 at 550 nm, and 1.46 at 365 nm; and cloud

optical depth was unity at a pressure of ~50 mb. This was the key information that made it possible to identify the composition of the cloud as concentrated sulfuric acid droplets.

Subsequent polarimetry observations from the Cloud Photopolarimeter (CPP) experiment on the Pioneer Venus spacecraft in a nearly polar orbit about Venus have confirmed this general picture and provided further spatial and temporal coverage unattainable in ground-based observations. Analyses of CPP polarimetry reveal that, in addition to the main cloud of 1-μm radius sulfuric acid droplets, an extensive haze of submicron-sized (~0.2 μm) aerosols extends above the main cloud primarily in the polar regions and exhibits a substantial temporal variation in optical thickness (Travis et al., Science 203, 781, 1979; Kawabata et al., J. Geophys. Res. 85, 8129, 1980).

The principal reason for the effectiveness of remote sensing by polarization measurement is the significantly greater sensitivity of polarization to particle size and optical properties than is the case for intensity. Some aspects of this behavior are illustrated in Figure 1, where the normalized intensity and percent linear polarization are compared for single scattering of unpolarized light by spherical particles of refractive index 1.33 (appropriate for water at visible wavelengths). Contours of constant polarization and intensity show the relative dependence of cloud features on phase angle (sun-object-observer angle) and size parameter. (Size parameter, which is the ratio of particle circumference to the wavelength of light considered, is used as the reference coordinate because scattering properties depend on the ratio rather than the physical size of the particles.) At larger size parameters, the sharp peak in polarization near 35° phase angle is characteristic of the rainbow feature of spherical particles (located at ~42° phase angle for very large particles such as raindrops). Although maximum intensity also occurs at that phase angle, it is not as sharply defined as the polarization feature, and becomes even less discernible when multiple scattering effects are taken into account. The single scattering features of polarization are characteristically less subject to "dilution" by multiple scattering (cf. Hansen and Travis, Space Sci. Rev. 16, 527, 1974) and thus, in contrast to intensity, retain more information content.

1.3 MEASUREMENT METHOD

The EOSP instrument will make polarization and intensity measurements of the Earth at 12 visible and near-infrared spectral bands selected for maximum sensitivity to cloud and aerosol features. The scanning mirror assembly of EOSP will sweep the 14-mrad instantaneous field of view (IFOV) in the cross-groundtrack direction with a scan rate such that the 10-km IFOV footprints at nadir for successive scans are contiguous. Samples every 14 mrad in scan angle will give approximately 180 scan elements from limb to limb. A key aspect of polarimetric

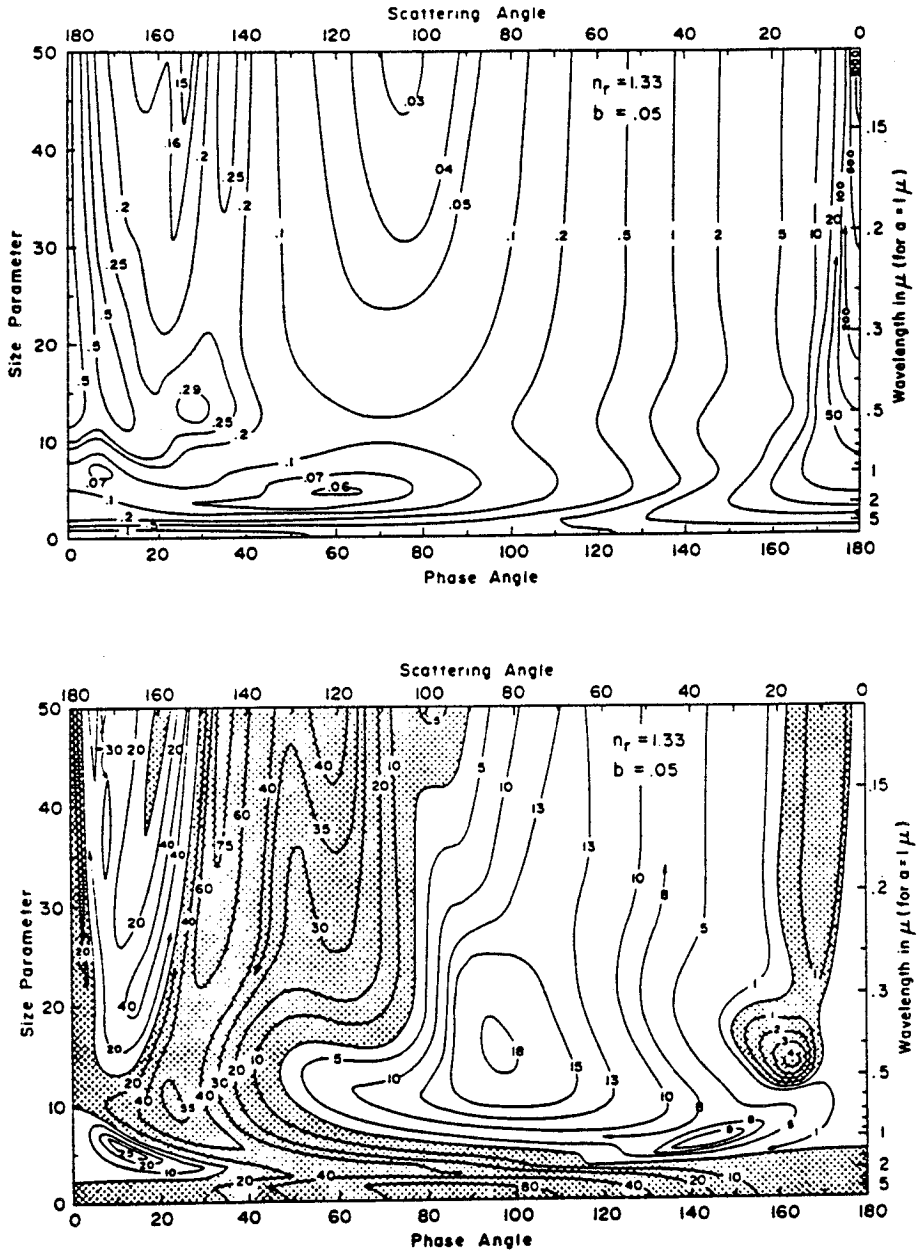

Figure 1. Comparison of particle size discrimination by polarimetry and photometry. *Lower panel: contour diagram of the percent polarization for single scattering of unpolarized light by spherical particles of refractive index 1.33. Shaded areas correspond to positive polarization, i.e., the intensity in the plane of scattering is smaller than that in the perpendicular plane; unshaded areas indicate negative polarization values. Size parameter is $2\pi a/\lambda$, where a is the effective mean radius (and b=0.05 indicated in the figure, the effective variance) for a gamma distribution which represents a dispersion of sizes to simulate natural conditions (cf. Hansen and Travis, Space Sci. Rev. 16, 527, 1974). Upper panel: the same as below, except that the contours are for the normalized intensity.*

observations is the information content that is provided by variations with viewing geometry, particularly phase angle. Figure 2 displays contours of phase angle for the observed points in EOSP scans as a function of scan element and subspacecraft latitude for a solar declination of 0°, i.e., the equinoxes. While there is a latitudinal shift in the contours with season, the essential features remain similar: middle phase angles (~80°) towards the west and smallest phase angles near 10 - 20° somewhat east of nadir at low latitudes. As indicated below, the phase angle coverage that is obtained with the proposed Eos sun-synchronous orbit is quite appropriate for achieving the EOSP scientific objectives.

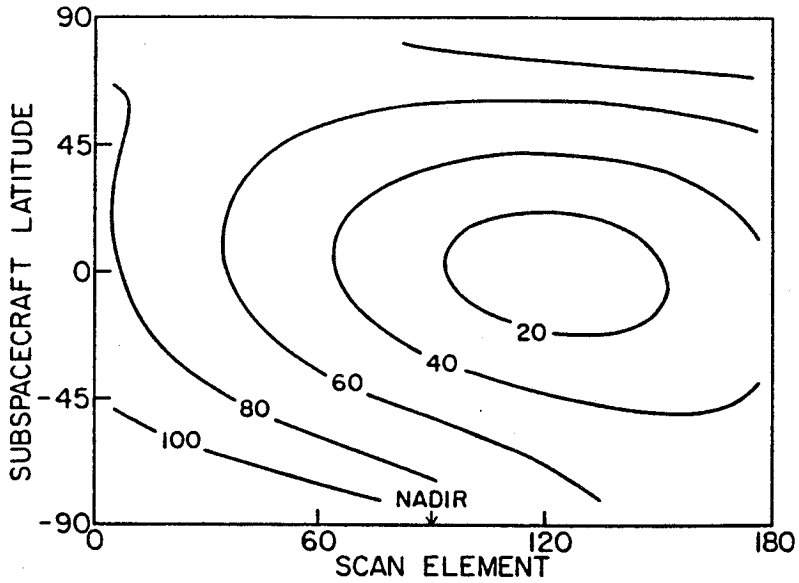

Figure 2. Contours of phase angle for observed points in EOSP scans. *Phase angles are shown as a function of scan element and subspacecraft latitude for Eos polar platform with 1:30 p.m. equator crossing time. Scan element zero corresponds to the west limb, 90 to the nadir direction, and 180 to the east limb.*

The first step in the systematic interpretation of EOSP measurements is to characterize the observed regions into cloudy and cloud-free areas. While the obvious expectation of higher radiances for cloudy regions in typical satellite images might lead the unwary to conclude that such a step is trivial, existing cloud climatology schemes using only visible wavelength radiances must employ sophisticated algorithms and ancillary data to distinguish clouds (Rossow et al., J. Clim. Appl. Meteor. 24, 877, 1985). The first cloud algorithms used differences in the characteristics of the spatial and temporal variability of monochromatic intensities to distinguish between cloudy and clear conditions; more recent methods have begun to use multispectral intensities. For cloudy regions, a primary objective is the determination of the total cloud optical thickness and cloudtop height. Traditional methods rely on the fact that to first order, higher radiance

levels correspond to optically thicker clouds. Such an approach is frequently subject to ambiguity unless supplemented with additional information, for example, thermal infrared band measurements to indicate the cloudtop temperature and thus estimate the altitude of the cloudtop.

Since very little spectral intensity and no polarimetry measurements exist covering the whole Earth over seasonal time scales, little use has been made of and little information exists to develop cloud and aerosol discrimination techniques. Thus, the analysis strategy of the EOSP science team will have two phases. In the first, a "cloud" algorithm will be used to divide the data into the two optical depth ranges that generally separate water clouds from other aerosols using intensities and polarization information in the 12 EOSP spectral bands. Depending on phase angle, polarization is usually a more sensitive measure of optical thickness than is the intensity (cf. Hansen, J. Atmos. Sci. 28, 1400, 1971). Polarization measurements are particularly useful in detecting optically thin clouds which often present major difficulties for traditional algorithms. Taken together, the multiband intensity and polarization measurements will permit much tighter constraints on the inferred cloud optical thickness than can be achieved with intensity data alone. The use of this initial cloud algorithm in phase one facilitates the further analysis of the spectral and polarimetric information by providing a first order discrimination of different aerosol types and differentiating between single and multiple scattering regimes. This division into cloudy and "clear" will also facilitate investigation of the surface spectral polarimetric properties. Based on the analysis of the results of the first phase, a second phase analysis can be performed with an enhanced algorithm that has been extended to use additional spectral and polarimetric signatures to refine the discrimination of various cloud and aerosol types and their optical properties. The key to this approach is to perform the first phase analysis in a fashion such that phase two adds information without repeating the earlier processing.

At shorter wavelengths in the visible, Rayleigh scattering from the molecules in the atmosphere can dominate the observed polarization at moderate phase angles ($\gtrsim 50°$). In Figure 3 the varying effects of Rayleigh scattering for different cloudtop pressures are shown for the 410-nm EOSP band. The top panel presents the computed polarization signature as a function of scan element for a uniform cloud of 10-μm radius water droplets having an optical thickness of 10 with the cloudtop at 500 mb. The sharp peak at a phase angle slightly less than 40° is the rainbow feature, while the strong increase for phase angles greater than about 70° is due entirely to Rayleigh scattering. Since the Rayleigh scattering optical thickness above the cloud top is proportional to the cloudtop pressure, the relative effect will vary accordingly. The lower panel illustrates this with curves representing the differences in percent polarization between that for the 500-mb cloudtop and the results for 400, 300 and 200 mb. For example, at a phase angle of about 80°, the 15.5% polarization for the 500-mb cloudtop is approximately 7.5% greater than

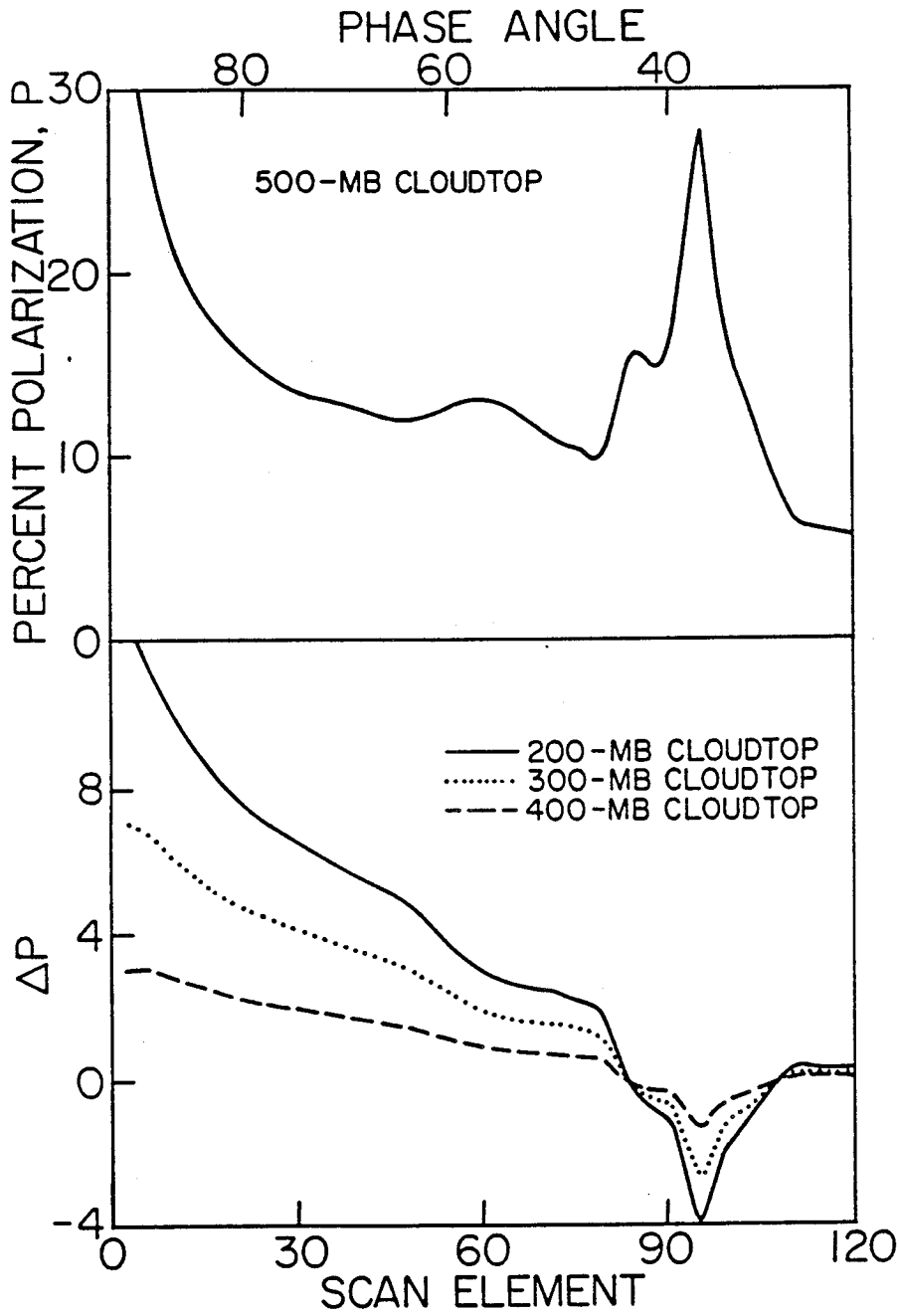

Figure 3. Varying effect on polarization of Rayleigh scattering for different cloudtop pressures for the 410-nm EOSP band. *Top panel: a scan for subspacecraft latitude of 30°S simulating the percent polarization (P) at 410 nm that would be observed for a uniform cloud of optical thickness 10 and cloudtop pressure level of 500 mb composed of 10-μm radius water droplets with a size distribution of effective variance 0.15. Scan element zero corresponds to the west limb and 90 to the nadir direction. Bottom panel: difference in percent polarization between the 500-mb cloudtop model and models for 400, 300 and 200 mb, i.e., ΔP = P(500 mb) - P(indicated cloudtop pressure).*

that for the 200-mb case. Since the expected accuracy of EOSP polarization measurements is better than 0.2%, the determination of the pressure level of the top of water clouds at observed points with phase angles greater than about 50° should be straightforward and quite sensitive.

A series of aircraft observations of the polarization of reflected sunlight from terrestrial clouds were made by Coffeen and Hansen (Proc. Eighth Intl. Sympos. Remote Sens. Environ., Univ. Michigan Press, 1972) for a number of different cloud systems. They found distinct rainbow features in the polarization for all clouds observed at the appropriate phase angles and known on the basis of altitude and visual appearance to be water rather than ice. To no surprise, cirrus clouds exhibited no rainbow but showed instead a broad positive polarization feature covering a wide range of middle phase angles. Figure 4 shows this striking difference in polarization signature between ice and water clouds as illustrated for typical cirrus cloud and altocumulus clouds. The ease with which the particle phase at the top of clouds observed at phase angles in the 35 - 45° range is apparent, where the absence of a rainbow feature means ice particles.

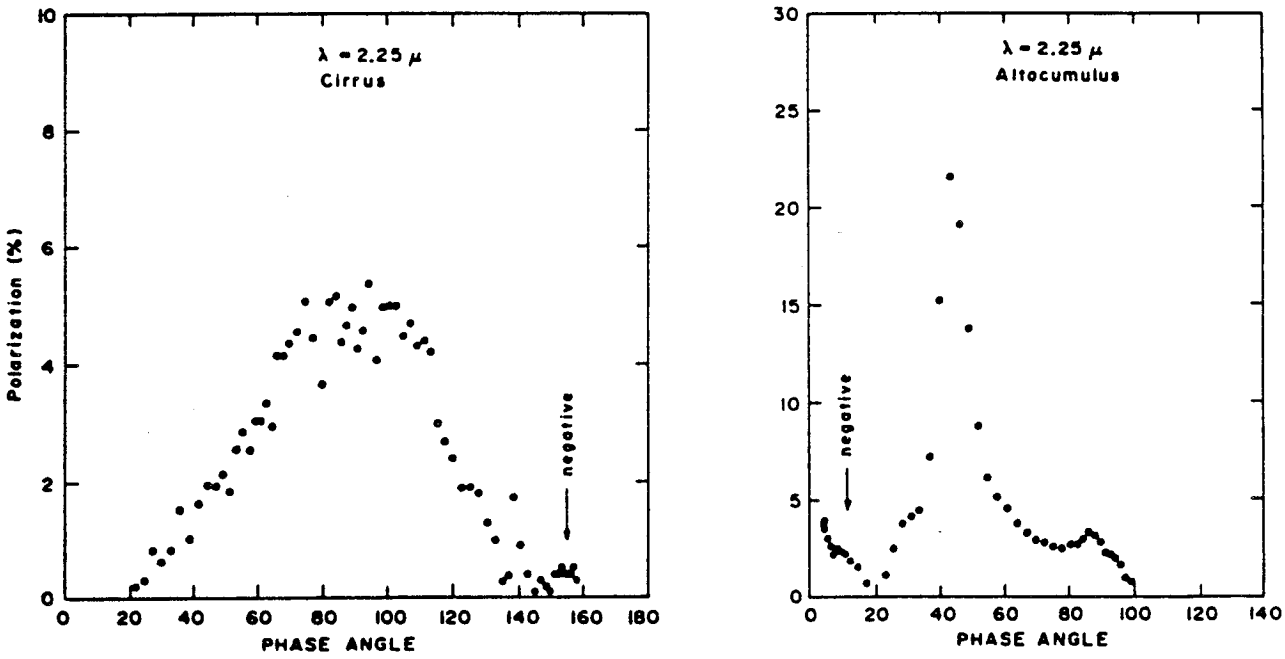

Figure 4. Illustration of cloud type discrimination from polarimetric measurements. *Percent polarization of reflected sunlight observed at a wavelength of 2.25 μm for a cirrus cloud (left) and an altocumulus cloud (right) from aircraft measurements by Coffeen and Hansen.*

For water clouds, the strength and precise location in phase angle of the rainbow feature in the polarization determine cloud particle size. Figure 5 displays the polarization degree for the

2.25 μm band as a function of scan element simulated using multiple scattering models for uniform clouds of optical thickness 10 and with particle sizes of 5 and 10 μm, respectively. These simulated scans were calculated for the viewing geometry corresponding to a subspacecraft latitude of 30°S (cf. Figure 2). The cloud with 10-μm radius particles has a rainbow feature with a peak polarization of more than 9% at a phase angle of ~37° (scan element 94), while the 5-μm case exhibits a rainbow centered at about 32° phase angle (scan element 107) with a significantly lower polarization degree. This behavior is a result of the sensitive dependence of the single scattering characteristics for the rainbow feature at this range of size parameters (~14 for the 5-μm particles and 28 for 10 μm; cf. Figure 1). The 2.25-μm band was selected specifically to obtain this sensitivity for particle sizes typical of water clouds. In practice, this determination of particle size requires a cloud system that is uniform over a region large enough (~30 scan elements, or 300 km) so that the phase angle of the peak of the rainbow feature can be discerned.

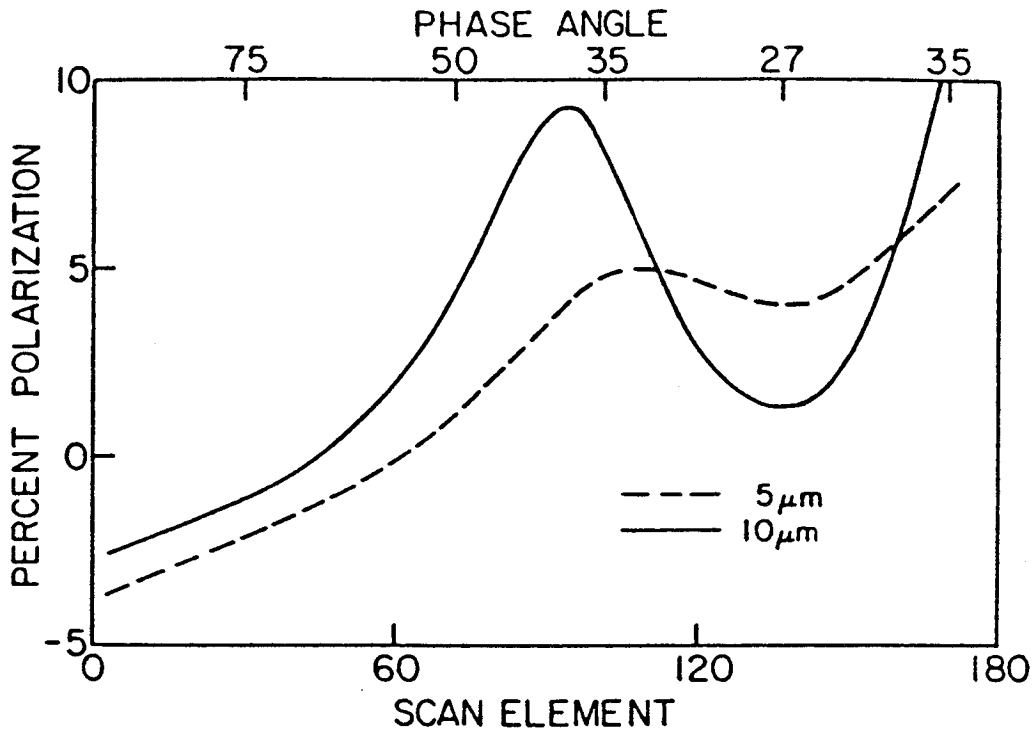

Figure 5. Cloud particle size discrimination from polarimetric measurements. *Percent polarization at a wavelength of 2.25 μm corresponding to a simulated EOSP scan at subspacecraft latitude 30°S for uniform clouds of optical thickness 10 and with mean cloud droplet radii of 5 μm (dashed line) and of 10 μm (solid line), respectively.*

In cloud-free regions, the focus of the EOSP experiment turns to a characterization of the background aerosol component of the atmosphere. Existing techniques for deriving aerosol optical thickness from satellite observations generally rely on visible wavelength radiances. One method uses the increase in the observed radiance due to greater scattering of sunlight from optically thicker aerosol layers, inferring the optical thickness from radiative transfer modeling and/or empirically derived relations (cf. Koepke and Quenzel, J. Geophys. Res. 84, 7847, 1979; Fraser et al., Atmos. Environ. 18, 2577, 1984). Another approach is based upon the decrease in contrast of surface features with increasing aerosol optical thickness (cf. Kaufman and Joseph, J. Geophys. Res. 87, 1287, 1982). Both methods have characteristic limitations. The former requires very accurate knowledge of the surface albedo and is dependent on the absolute radiometric calibration of the observed radiance. This method is best suited for regions with uniform and low surface albedo, such as for the ocean (but well away from the sun glint region). The latter method, however, is predicated on sharp changes in surface albedo such as that corresponding to a coastline, river, etc., and thus requires substantially higher spatial resolution.

As is the case for clouds, the measurement of polarization (in addition to radiance) is the key information for the accurate determination of the optical properties of aerosol layers. Because the polarization degree is a relative measurement of the difference of intensities in orthogonal planes compared to the total intensity, it is independent of the absolute radiometric calibration. As a consequence, absolute calibration uncertainty, which is the major source of error for methods utilizing only the radiance, does not affect the interpretation of polarimetric observations of aerosols. Moreover, the uncertainty in surface albedo also has no adverse impact unless the optical thickness of the aerosol layer is extremely small and the sunlight reflected from the surface is strongly polarized.

Determination of the aerosol optical thickness will be based on the characteristic behavior of polarization, i.e., optically thinner layers exhibit higher polarization degree because there is less dilution of the single scattering signature by multiply scattered photons. This effect is particularly evident for the range of optical thickness expected for typical aerosol layers, viz., 0.01 to 1. The mean particle size for aerosols is usually on the order of 1 μm or less. As a consequence, the scattering efficiency of aerosols has a strong wavelength dependence, being lower at near-infrared wavelengths than in the visible. This wavelength dependence of the optical thickness of the aerosol layer can be used to advantage to maximize the sensitivity of the retrieval procedure for determining the optical thickness and also to determine the particle size characteristics.

Crude height information regarding the top of tropospheric aerosol layers can be addressed by the same type of approach employed for determining the cloudtop pressure level for water

clouds. The 410-nm EOSP band will always have significant polarization due to Rayleigh scattering at phase angles of order 50° or more. However, in contrast to the case for water clouds, aerosols present a situation in which the particle optical properties (refractive index) may not be known a priori. The actual analysis will therefore need to involve to some degree of simultaneous determination of the particle size and optical properties, specifically, refractive index and single scattering albedo. Under these circumstances, it is expected that development of specific procedures which will permit the routine determination of these properties will evolve from the compilation of adequate statistics on aerosol characteristics based on observations with the EOSP.

A significant by-product of the characterization of the aerosol optical properties is the resulting information that is needed to perform accurate atmospheric corrections for land and ocean observations. Ideally, such corrections involve some radiative transfer modeling to completely describe the scattering and diffuse transmission due to the atmosphere and aerosols. However, such an approach requires a reasonably precise specification of the aerosol optical properties. Given the regional and temporal variability of the aerosol component of the atmosphere, accurate atmospheric corrections have been practical only for limited circumstances.

The ideal approach for deducing the atmospheric correction would involve first determining the mean particle size, single scattering albedo, refractive index, and aerosol optical thickness from the analysis of EOSP observations. Then, these properties could be input into detailed multiple scattering models to iteratively deduce the multispectral intensities corresponding to the surface reflectance. However, such an effort is sufficiently computer intensive to be of limited value for routine atmospheric correction for large observational data sets covering extensive regions. Rather, the EOSP science team will develop retrieval techniques based upon establishing the key observations which permit a general characterization of the aerosol effects. Detailed computations will be used to verify the retrieval strategy and parameterizations for a limited number of typical situations. The compilation of a global aerosol climatology is an essential goal of this effort. As the actual variability of aerosol characteristics and distribution is understood, it will become feasible to develop reliable and accurate techniques for atmospheric correction that are practical for routine application.

The application of polarimetry for remote sensing of clouds and aerosols, while limited, is nevertheless a proven concept. In contrast, little has been done with respect to vegetation and land polarization observations. The only terrestrial polarimetry from space to date are preliminary measurements using photography through polarization analyzers performed by Shuttle astronauts. The typical spatial scales of interest for classifying land and vegetation features are usually much smaller than the EOSP IFOV footprint of 10 km (at nadir). It is thus likely that

interpretation of EOSP polarimetry observations will be most meaningful when the type of vegetation or land feature is relatively uniform over the EOSP IFOV. In this regard, an examination of the variability of radiance within the EOSP IFOV based on the higher resolution MODIS or HIRIS data should provide some guidance. Though the EOSP spatial resolution may be less than ideal for this type of observation, the relative ease with which global surveys will be obtained for simultaneous polarimetry at 12 different wavelengths should help to establish the value of polarimetric measurements in land and vegetation monitoring.

An accurate determination of the polarization degree of the sunlight reflected from the surface will be strongly coupled to the atmospheric correction process because of the contribution to the observed polarization from the aerosols and molecular scattering. In fact, for thicker aerosol layers, the surface polarization characteristics may well be masked. Even if we should find it difficult to derive significant additional information on land or vegetation characteristics from the surface polarization, a systematic compilation of its variability will be useful in estimating errors associated with making atmospheric corrections which neglect the surface polarization signature.

Section 2
INSTRUMENTATION

2.1 INSTRUMENT OVERVIEW

Key Instrument Features. To accomplish the scientific objectives a polarimeter is required that has the following key features:

1. simultaneous detection of orthogonal linear polarization components of the scene radiance;
2. capability to interchange the roles of corresponding detector elements used to detect orthogonal polarization components;
3. spatial coverage from limb to limb to provide global polarization maps;
4. simultaneous measurement in all the spectral bands of interest;
5. simultaneous measurement of the 0°/90° and 45°/135° pairs of linear polarization components;
6. instrumental polarization that is both small and varies only slightly with scan angle with a method to measure the instrumental polarization in flight as well as pre-flight;
7. single instantaneous field of view for the above measurements to assure automatic spatial registration of the polarimetric data; and
8. inflight calibration sources and methods adequate to provide radiometric calibration and polarimetric calibration (see also Items 2, 5, and 6).

Item 1 is essential to achieve the desired polarimetric accuracies of ~0.1% for low polarization (<10%) scenes. If simultaneous detection of orthogonal polarizations if not done, then "false polarization" can be expected to limit the accuracies to approximately 1%. False polarization results when intensity changes due to viewing slightly different fields of view are erroneously transformed into apparent polarimetric changes. This is of such fundamental importance that this approach has been used on all polarimeters with which the EOSP team members have been associated. The implementation approach used to obtain this simultaneity is the use of a Wollaston prism to spatially separate orthogonal linear polarization components.

Item 2, the capability of cross-calibrating detectors used to measure the orthogonal polarization components, is another essential feature of the EOSP. This capability is obtained through the use of a halfwave retarder oriented sequentially during calibration at position angles separated by 45°, which effectively interchanges the roles of equivalent detectors located in the two orthogonally polarized beams of the Wollaston prism. This feature of the EOSP permits maintaining the inherent polarimetric accuracy even in the presence of slow, differing changes of channel responsivities with time, temperature, radiation, etc.

Item 3 is critical to achieving both the global spatial coverage and wide phase angle coverage needed to achieve the scientific goals enumerated in the previous section. Due to deficiencies, e.g., variation of instrumental polarization with scan angle and/or large instrumental polarization, resulting when a scan mirror is used, either rotation of the entire telescope or a method to reduce instrumental polarization and its variation with scan angle is required. For EOSP a compensated, two-mirror scanning approach has been selected which has the same angle of incidence at both mirrors for all scan angles and the planes of incidence arranged to be orthogonal for polarization compensation.

Implementation of the simultaneous spectral measurements of Item 4 allows more efficient use of observing time, while also avoiding non-registration of spatial and spectral scene samples. Without this approach, even if spatial and spectral registration were achieved with nominal orbit and scanning parameters, any changes would modify this registration and reduce the scientific utility of the scene data.

The 0°/90° and 45°/135° measurements of Item 5 are required to obtain full characterization of the scene intensity and linear polarization. The desire for simultaneity of these two sets of measurements is analogous to the spectral simultaneity requirement in that it improves measurement efficiency and assures spatial registration of the required polarimetric components. The lack of such spatial registration would reduce the polarimetric accuracy, although much less than would result from false polarization without the Item 1 feature.

Item 6 is important since with large (more than a few percent) or varying instrumental polarization, significant error can be introduced when attempting to correct scene data. While the variation of instrumental polarization with scan angle can be measured during pre-flight testing, any changes, such as, altered optical properties of the scan mirrors due to contamination, are more difficult to characterize in flight. Thus, judicious instrument design is essential to minimize of the variation of instrumental polarization with scan angle. The compensated, two-mirror method selected for EOSP satisfies this constraint, while achieving the scanning requirements of Item 3.

The single IFOV of Item 7 assures uncomplicated and consistent correlation of the spatial/spectral polarimetric data. Multiple, non-aligned IFOVs would complicate sample registration, since the scanning method selected to satisfy Item 6 and the limb-to-limb coverage of Item 3 produces image (and polarization) rotation as well as footprint growth (as compared to the IFOV footprint at nadir).

Item 8 involves two distinct types of inflight calibration, radiometric and polarimetric. The radiometric calibration is needed to convert the sensor outputs to equivalent scene radiance

values with an absolute accuracy of 5% or better (design goal 3% or better). As a minimum, a means to track any responsivity change from the final pre-flight radiometric calibration through the duration of the mission is required. The key elements of the polarimetric calibration are achievable by virtue of the implementation of Items 2, 5, and 6. To achieve the desired absolute polarimetric accuracies (0.1% for polarizations of 10% or less), it is important to have an on-board source (or solar input) of low polarization to track any changes, e.g., scan mirror reflectance changes, that alter the instrumental polarization.

Summary Description of Instrument. Figure 6 shows a cut-away view of an instrument design that satisfies all the requirements imposed by the science goals. The basic instrument parameters are summarized in Table 1. Details of the EOSP design are discussed in the sections that follow. Throughout the design, heavy emphasis has been placed on simplifying the design where possible and on using proven techniques and existing space-qualified hardware. These approaches will minimize both development and cost risk and enhance overall system reliability.

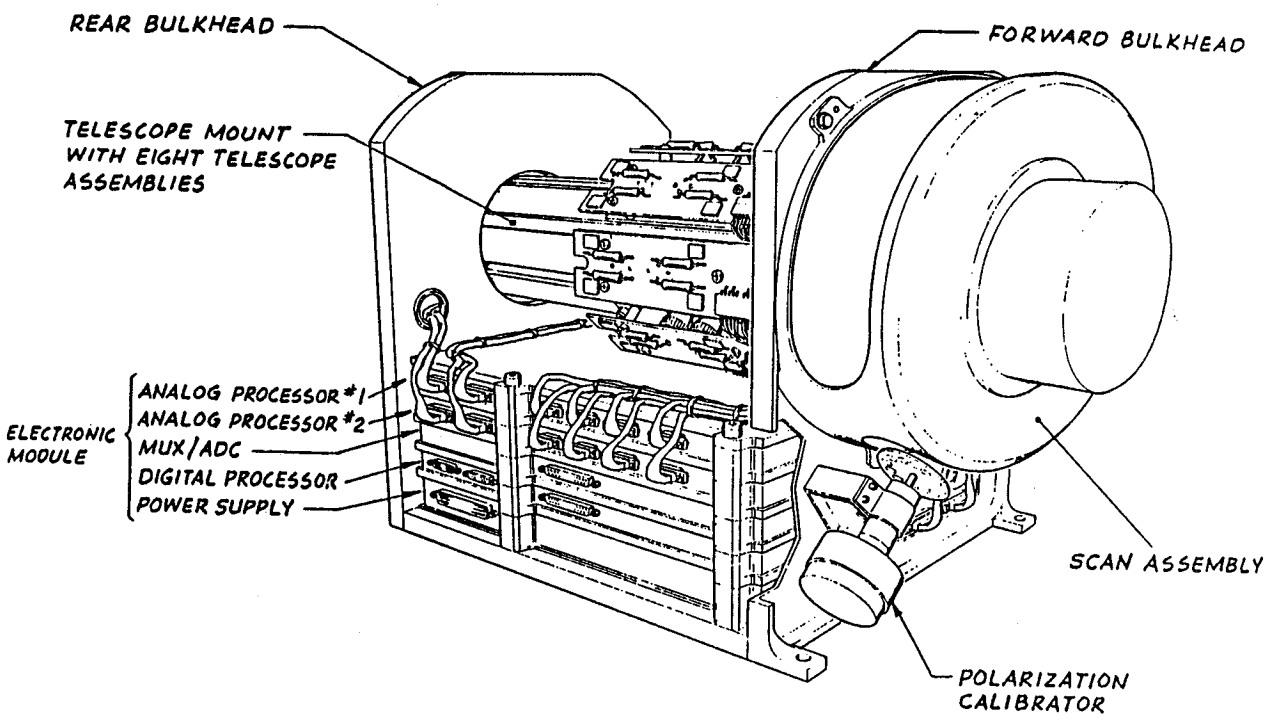

Figure 6. Cutaway view of the EOSP as viewed from the inboard side of the spacecraft.

Table 1. EOSP Instrument Parameter Summary

PARAMETER	INSTRUMENT CONFIGURATION
Scan Method	Polarization-Compensated, Twin-Mirror Scanning (Cross-track) with Continuous Rotation at 40.5 rpm; Scene Scanned from Limb to Limb with DC Restoration and Cal Lamp Viewing during Non-Scene Portion of Scan
Scene Flux Collection	Eight Boresighted, 1-cm Aperture, f/5 Telescopes using Refractive Apochromatic Doublet Design
Instantaneous Field of View	Single Circular 14.2-mrad Field of View (10 km Nadir Footprint with a Platform Altitude of 705 km)
Spectral Bands	12 Spectral Bands; in the VINIR: 410nm ($\Delta\lambda$=30nm), 470nm ($\Delta\lambda$=20nm), 555nm ($\Delta\lambda$=20nm), 615nm ($\Delta\lambda$=15nm), 675nm ($\Delta\lambda$=20nm), 750nm ($\Delta\lambda$=15nm), 880nm ($\Delta\lambda$=20nm), 950nm ($\Delta\lambda$=20nm); in the SWIR: 1250nm ($\Delta\lambda$=60nm), 1600nm ($\Delta\lambda$=60nm), 2050nm ($\Delta\lambda$=100nm), and 2250nm ($\Delta\lambda$=100nm)
Spectral Separation Method	Dichroic Beamsplitters Plus Bandpass Filters to Separate Three Spectral Bands in Each Telescope/Relay Optics Assembly
Polarization Separation	Calcite Wollaston Prism Used in Each Telescope Assembly to Provide Simultaneous Measurement of Orthogonal Linear Polarization Components; Telescope Assemblies Paired, with the Two Assemblies Oriented at 45° to Each Other with the Pair Measuring the 0°/90° and 45°/135° Polarization Components in Three Spectral Bands
Detectors	32 Blue-Enhanced Silicon Photodiodes (Dual-Element Packages) for VINIR Bands; Cold Focal Plane with Eight Pairs of HgCdTe Photodiodes (2.5 μm Cut-off Wavelength) Cooled to 200 K or Lower for SWIR Bands
Detector Cooling	Simple, Single-Stage Radiative Cooler to Cool the HgCdTe Detectors to 200 K or Lower (180 K Nominal); Eight Commandable Set Points to Allow Accommodation for Degradation over Mission Life
Scene Sampling	All 48 Signal Channels Sampled Simultaneously for Each IFOV Sampled (3.3 ms Sample Period) with 180 IFOV Samples Collected Per Scan (Allowing Limb-to-Limb Measurements Plus Calibration and Pre/Post DC-Restore Dark Measurements)
Analog/Digital Conversion	14-Bit A/D Conversion of Each of the 48 Signal Channels
Data Rate	Maximum Data Rate in Measurement Mode including Housekeeping (Buffered Over 1.48 sec Scan Period) is 86 kbps; in Housekeeping Mode, 200 bps
Inflight Polarization Calibration	Each Pair of Telescope/Relay Optics Assemblies Uses One Achromatic Half-wave Retarder Positionable by 22.5° and 45° to Provide Responsivity Cross-Calibration Between Each Pair of Telescope Assemblies and Between the Detectors Measuring Orthogonal Polarization Components within Each Telescope Assembly; Additionally, the Polarization Calibrator Provides near 100% Linearly Polarized Inputs at Five Different Azimuths at Four Different Levels and near 0% Polarized Inputs at Eight Different Levels
Inflight Radiometric Calibration	Solar Diffuser with Two Reflectance Levels Positionable into Scanned Swath that is Solar Illuminated Near the South Pole (Reflective Surface Protected in Stowed Position); Four Calibration Lamps in Polarization Calibrator that can be Powered in Any Combination together with a Selectable Neutral Density Filter Providing Eight Radiance Levels
Measurement Accuracy	Absolute Radiometric Better Than 5% (Design Goal Better Than 3%); Polarimetric Accuracy Better Than 0.2% (Design Goal Better Than 0.1%); Signal-to-Noise Ratio Exceeds 2000 for All Bands when the Effective Albedo is 0.3 or Greater
Size/Mass/Power	Size (Excluding Solar Diffuser) 50 x 26 x 38 cm (track x cross-track x nadir) in Launch Configuration with Cross-track Dimension Increased to 50 cm with Radiative Cooler Earth Shield Deployed (Added Height of Solar Diffuser Structure ~30 cm for Clear Solar View); Mass 16.2 kg; Power 14 W Normal Operating, 9.5 W Standby Mode, and 22 W Peak

The scanning system provides a continuous cross-track scan motion that allows limb-to-limb viewing and dc-restoration plus calibration source viewing during the backscan portion of the 360° rotation. The twin scan mirror assembly design provides polarization compensation at all scan angles. Eight bore-sighted telescope/aft optics assemblies provide the required spatial, spectral and polarization separations of the scanned scene. Each assembly contains a baffle system, refractive telescope, field stop, relay lens, and Wollaston prism to define the field of view and separate the incident scene flux into two orthogonally-polarized, angularly-separated beams. These beams are spectrally separated into three spectral bands using two dichroic beamsplitters and three bandpass filters. Each pair of polarized and spectrally defined beams are focused on either a dual-detector, silicon photodiode detector package (for the visible and near infrared [VINIR] spectral bands) or a pair of HgCdTe photodiode detectors located on the cold (185K) focal plane (for the shortwave infrared [SWIR] spectral bands).

The telescope/aft optics assemblies are grouped in pairs with each pair covering three spectral bands (of the total of 12), with the octagonal telescope mount providing the proper orientation to allow simultaneous polarization sampling of the 0°/90° and 45°/135° polarization azimuths. Four achromatic halfwave retarders located on a retarder wheel provide occasional cross-calibration of the detectors used to measure the orthogonal polarization components. The halfwave retarder positioning for normal scene-viewing measurements is shown in part (a) of Figure 7, while the method for intra-telescope channel cross-calibration is illustrated in part (b). Similarly, the method for inter-telescope channel cross-calibration is shown in part (c) of Figure 7.

The calibrator assembly attached to the scan mirror assembly housing on the platform side of the mirror assembly axis (cf. Figure 6) provides a set of known source polarization and radiance outputs for an end-to-end inflight calibration. As illustrated schematically in Figure 8, the calibrator employs an eight-position wheel (each position viewed by one of the eight EOSP telescopes) illuminated by flux from eight exit ports of a small integrating cavity with four small tungsten filament lamps (with each lamp separately commandable to provide a range of radiance levels). In the polarization calibration mode, the wheel is stepped so that each telescope views each of the eight positions in turn. By performing this calibration cycle periodically, any changes in the apparent polarization degree and azimuths relative to the known source values can be used to deduce any polarimetric response changes, i.e., alteration of either the instrumental polarization or linear polarization responsivity.

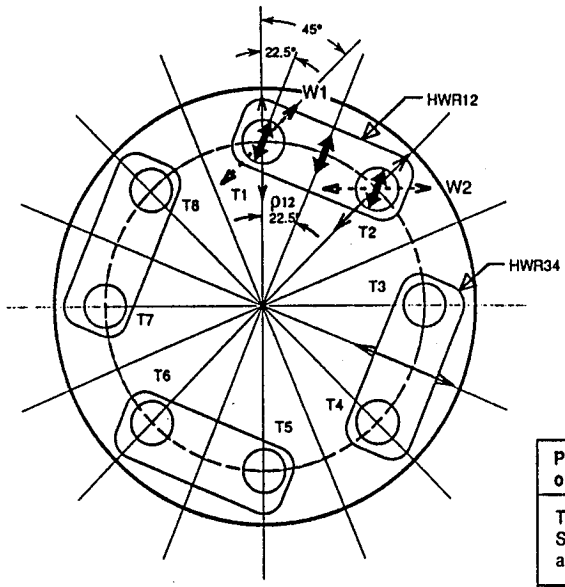

Normal Scene Measurement Positioning (ρ_{12} = +22.5°) of Retarder Wheel

Halfwave Retarder (HWR) Fast Axis Azimuth

P-Plane Azimuth of Telescope Beamsplitters

Azimuth of Wollaston Prism Plane of Deviation

Polarization Azimuth of Incident Flux	0° 90°	45° 135°
T1 Channel that Senses Flux Polarized at Specified Azimuth	$S_1(0°)$ $S_1(90°)$	Either Sensed Equally by $S_1(0°)$ by $S_1(90°)$
T2 Channel that Senses Flux Polarized at Specified Azimuth	Either Sensed Equally by $S_2(45°)$ & $S_2(135°)$	$S_2(45°)$ $S_2(135°)$

Figure 7(a). Halfwave retarder positioning for normal scene measurements.

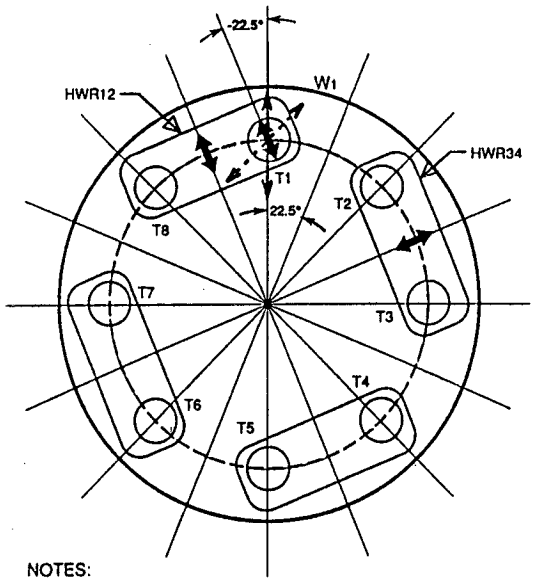

Intra-Telescope Channel Cross-Calibration Positioning (ρ_{12} = -22.5°) of Retarder Wheel for Telescopes T1 (and Simultaneously for T3, T5, and T7)

Telescope	Polarization Azimuth of Incident Flux	
	0° 90°	45° 135°
T1 Channel that Senses Flux Polarized at Specified Azimuth (Condition per Note 1)	$S_1(90°)$ $S_1(0°)$	Either Sensed Equally by $S_1(0°)$ & $S_1(90°)$
T2 Channel that Senses Flux Polarized at Specified Azimuth (Condition per Note 1)	Not Applicable for Position Shown; See Note 2 regarding T2 Channel Cross-Calibration	

NOTES:

1) Intra-Telescope Channel Cross-Calibration Condition Shown Represents Rotation by -45° from Normal Scene Measurement Position.

2) Rotation by +90° from Retarder Wheel Position Shown (+45° from Normal Scene Measurement Position) Provides Intra-Telescope Channel Cross-Calibration for Telescope T2 (and Simultaneously for T4, T6 & T8), i.e., When Lefthand End of Halfwave Retarder for T1 and T2 (HWR12) is Over T2.

Figure 7(b). Halfwave retarder positioning for intra-telescope channel cross-calibration.

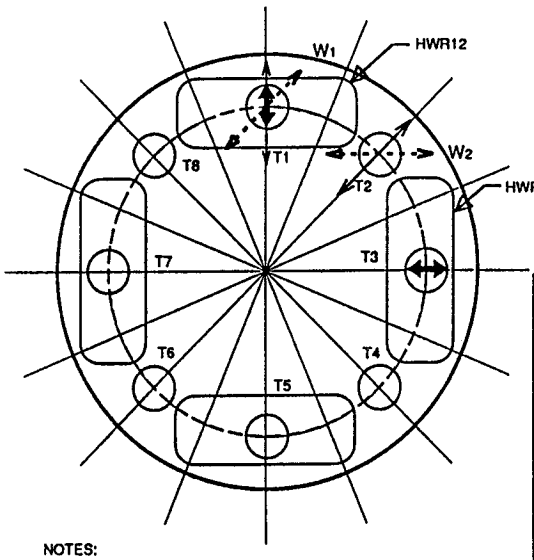

Inter-Telescope Channel Cross-Calibration Positioning (ρ_{12} = 0°) of Retarder Wheel for Telescopes T1 and T2 (and Simultaneously for T3 & T4, T5 & T6, and T7 & T8)

Telescope	Polarization Azimuth of Incident Flux	
	0° 90°	45° 135°
Azimuth Measured by T1 and T2 Channels with ρ_{12} = 22.5° (See Note 1)	$S_1(0°)$ $S_1(90°)$	$S_2(45°)$ $S_2(135°)$
Azimuth Measured by T1 Channels with ρ_{12} = 0 (See Note 2)	– –	$S_1(90°)$ $S_1(0°)$
Azimuth Measured by T2 Channels with ρ_{12} = 45° (See Note 3)	$S_2(135°)$ $S_2(45°)$	– –

NOTES:
1) Normal Scene Measurement Condition.
2) Provides Inter-Telescope Channel Cross-Calibration Condition (As shown in Figure).
3) Provides Inter-Telescope Channel Cross-Calibration Condition (Not Illustrated).

Figure 7(c). Halfwave retarder positioning for inter-telescope channel cross-calibration.

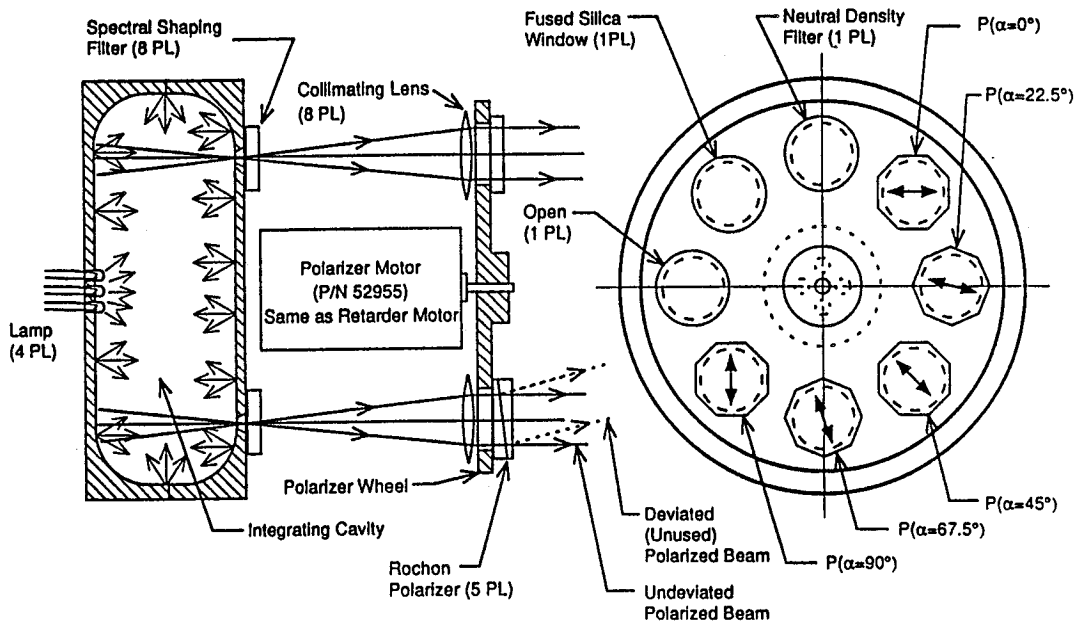

Figure 8. Schematic of the polarization calibrator assembly.

A simple, single-stage radiation cooler provides the required focal plane cooling for the HgCdTe detectors and associated preamplifiers. The radiation cooler earth shield in its launch configuration serves as a contamination cover. With the exception of the preamplifiers located with the optics, the remaining electronics (providing the signal processing and formatting, command and control, actuator driver circuitry, and power conditioning) are located in the electronics module portion of the instrument.

The solar diffuser will be mounted on a light-weight frame attached to the optics housing. Upon command the solar diffuser can be driven from its protected configuration into the scanned swath for solar calibration near the south pole.

2.2 SYSTEM MATHEMATICAL CHARACTERIZATION

It is convenient to describe the EOSP signal channels in terms of a Stokes vector/Mueller matrix formalism. The scene spectral radiance can be characterized in terms of the Stokes vector, usually denoted by {I, Q, U, V}, where { } denotes a column vector (see for example, W.A. Shurcliff, *Polarized Light-Production and Use*, Chap. 2, Harvard Univ. Press, Cambridge, Mass. (1962)). These components can be expressed in terms of measurements of the scene spectral radiance as

$$I = L_{0°} + L_{90°} = L_{45°} + L_{135°}$$

$$Q = L_{0°} - L_{90°}$$

$$U = L_{45°} - L_{135°}$$

$$V = L_{rcp} - L_{lcp}$$

where $L_{x°}$ are spectral radiance values measured with an ideal linear polarizer at azimuths x° relative to a selected reference direction, and L_{rcp} and L_{lcp} are similar measurements made with ideal right and left circular polarizers, respectively. For the scenes of interest the circular polarization is negligible, and with V set equal to zero, it is convenient to express the Stokes vector in the form

$$\begin{bmatrix} I \\ Q \\ U \\ V \end{bmatrix} = \begin{bmatrix} L_{0°} + L_{90°} \\ L_{0°} - L_{90°} \\ L_{45°} - L_{135°} \\ 0 \end{bmatrix} = \begin{bmatrix} L_u + L_p \\ L_p \cos 2\alpha \\ L_p \sin 2\alpha \\ 0 \end{bmatrix}$$

where L_u is the unpolarized portion of the scene spectral radiance, L_p is the linearly polarized fraction of the scene spectral radiance, and α is the azimuth of the linearly polarization

component relative to the selected reference direction. In this case, the degree of linear polarization, $P = L_p/(L_u + L_p)$ and azimuth, α, are given by

$$P = \frac{\sqrt{Q^2 + U^2}}{I} \text{ and}$$

$$\alpha = \frac{1}{2} \arctan (U/Q).$$

While radiance values at four different azimuths are shown in the expressions for the equivalent data sets, i.e., the I, Q, U, the L_u, L_p, α, and the I, P, α sets, only three of the measurements are independent. For example, $L_{135°}$ can be eliminated from the I, Q, U data set, since

$$U = L_{45°} - L_{135°} = 2L_{45°} - I = 2L_{45°} - L_{0°} - L_{90°}.$$

The Mueller calculus is convenient to represent the modifications to the Stokes vector produced by transmission through one or more optical elements.(ibid., Chap. 8). In general, a 4 by 4 element transmittance Mueller matrix [M] relates the resultant output Stokes vector {I*, Q*, U*, V*} to the Stokes vector of the incident beam, i.e.,

$$\begin{bmatrix} I^* \\ Q^* \\ U^* \\ V^* \end{bmatrix} = [M] \begin{bmatrix} I \\ Q \\ U \\ V \end{bmatrix}$$

With an actual sensor system, the final form of the measured quantities usually are voltages or data numbers (DN), and it is useful to characterize each polarimeter channel by a system Mueller matrix [M_S] that has units of spectral radiance responsivity, e.g., DN per unit of spectral radiance. In this case, the vector $\{S_0, S_1, S_2, S_3\}$ representing the system output is given by

$$\begin{bmatrix} S_0 \\ S_1 \\ S_2 \\ S_3 \end{bmatrix} = [M_S] \begin{bmatrix} I \\ Q \\ U \\ V \end{bmatrix} = [M_S] \begin{bmatrix} L_u + L_p \\ L_p \cos 2\alpha \\ L_p \sin 2\alpha \\ 0 \end{bmatrix}$$

where the assumption of no circular polarization in the scene is explicitly included in the Stokes vector of the scene. For an perfect polarimeter consisting of an object-space scan system and

telescope that do not modify the scene polarization, plus a positionable, ideal halfwave retarder followed by an ideal polarizing beamsplitter, the system matrix M_S is given by

$$[M_S] = R_x T_x [P(\phi)] [R(\pi,\rho)]$$

where: R_x and T_x are the system responsivity and system optical transmittance, respectively, for channel "x", e.g., 0° or 90°; $[P(\phi)]$ is the Mueller matrix for an ideal linear polarizer oriented with transmission axis at azimuth ϕ to the reference direction; and $[R(\pi,\rho)]$ is the Mueller matrix for an ideal halfwave retarder, i.e., with retardance $\Delta = \pi$. For telescopes with the transmitted beams exiting the Wollaston having polarization azimuths parallel and perpendicular to the instrument reference direction (normal to baseplate), i.e., telescopes T2, T4, T6 and T8, matrix multiplication yields

$$[M_S] = \frac{R_x T_x}{2} \begin{bmatrix} 1 & \pm(\cos^2 2\rho - \sin^2 2\rho) & \pm 2\cos 2\rho \sin 2\rho & 0 \\ \pm 1 & \cos^2 2\rho - \sin^2 2\rho & 2\cos 2\rho \sin 2\rho & 0 \\ 0 & 0 & 0 & 0 \\ 0 & 0 & 0 & 0 \end{bmatrix}$$

where ρ is the orientation of the halfwave retarder fast axis and the upper sign corresponds to ϕ=0° and the lower sign to ϕ=90°. Thus the measured signals, i.e., corresponding to the intensity or S_0 term, for these telescopes (when scene circular polarization is negligible) are given by

$$S_{0,x}(\rho) = \frac{R_x T_x}{2} \left\{ I \pm Q(\cos^2 2\rho - \sin^2 2\rho) \pm 2U\cos 2\rho \sin 2\rho \right\}$$

For normal scene measurement where ρ=22.5°, the two channel signals are

$$S45(22.5) = \frac{R_{45}T_{45}}{2} \{I + U\} \text{ and } S135(22.5) = \frac{R_{135}T_{135}}{2} \{I - U\}.$$

where the simplified representations of $S45(\rho)$ for $S_{0,45°}(\rho)$, etc. have been used. Assuming that the relative value of responsivity constants are known from a polarimetric calibration of the instrument (cf. Figure 7(b)), the determination of U follows from the above equations. The corresponding signals for the channels in telescopes T1, T3, T5 and T7 are given by

$$S0(22.5) = \frac{R_0 T_0}{2} \{I + Q\} \text{ and } S90(22.5) = \frac{R_{90}T_{90}}{2} \{I - Q\}.$$

which permit the determination of Q in a similar fashion. The calculation of P and α from these measurements requires knowledge of the inter-telescope responsivity factors (cf. Figure 7(c)) among the four channels. Finally, the calculation of the absolute value for I requires an absolute determination of the responsivity constants, i.e., a radiometric calibration of the instrument channels.

For an actual instrument there will be small departures of the components from the ideal. For the EOSP the only departures expected to be significant (and therefore needing calibration) are expected to be small retardance variations of the halfwave retarder, small net polarization and retardance of the polarization-compensated scan mirror system, and possibly very small systematic positioning errors of the halfwave retarder azimuth.. If such departures from an ideal polarimeter are present, some of the elements of the system Mueller matrices for the channels will contain small correction factors. Proper characterization of these is the function of the pre-flight and inflight polarimetric calibrations.

2.3 OPTICAL DESIGN

Polarization Separation Method. Of the various types of polarimeters, a fundamental difference in approach and design exists between those which use a birefringent analyzer and two detectors to simultaneously measure two components of the incident beam, and those measuring only a single intensity for several analyzer positions. Since the latter uses only one detector, the analyzer is typically a dichroic element that transmits one of the linearly polarized components and absorbs the other. In spite of the detector cross-calibration required for two-detector, birefringent systems, the accuracy of such systems has been demonstrated to be clearly superior to that of dichroic polarimeters (Coffeen, p. 189 *Planets, Stars and Nebulae Studied with Photopolarimetry*, ed. Gehrels, Univ. of Arizona Press, 1974). The important distinction between the two basic types of polarimeters arises whenever a change in the observed scene radiance occurs between measurements at different analyzer orientations. For single-detector polarimeters, such a variation in scene radiance results in a contribution to the apparent polarization degree which is in fact a false polarization; however, little or no such error is generated for a two-detector, birefringent polarimeter. Such false polarization is a serious flaw for single-detector types of polarimeters if it cannot be assured that exactly the same scene area is viewed during the measurement of each polarization component, and it can be expected to limit the polarimetric accuracy to on the order of 1% at best for typical scenes of interest here. In contrast, the approach selected for the EOSP utilizing two Wollaston prisms oriented at 45° to each other to analyze the scene flux is virtually immune from false polarization effects.

Spectral Separation Alternatives. Several different methods of spectral separation were evaluated for use on the EOSP. In all cases the spectral separation was assumed to occur following the polarimetric analyzer, since spectral separation techniques typically have an associated polarimetric dependence, e.g., variation of grating efficiency with polarization as well as wavelength. The spatial/spectral simultaneity requirements resulting from the spatial coverage (scanning capability) requirement for the EOSP eliminate approaches that use sequential spectral sampling, such as the stepped filter wheel as used on the Galileo PPR. Similarly, the sequential sampling in interferogram space required in a Fourier transform spectrometer approach, e.g., using a birefringent interferometer, is not compatible in any simple manner with the EOSP scanning and spectral/spatial simultaneity requirements.

Spectral separation using dispersive approaches with gratings or prisms (or a combination) is compatible with the basic EOSP requirements. To cover the 400 nm to 2.25 μm spectral range would require multi-order usage of a grating with a means to select the desired orders or the use of more than one grating. Order selection could employ: (1) order filters if non-continuous spectral coverage is adequate (since overlapping orders occupy the same physical location); (2) dichroic beamsplitter(s) if near continuous spectral coverage is desired (with a spectral gap at the dichroic transition spectral region); or (3) cross dispersion using a second dispersive element (such as prism or grating). The use of prisms avoids the problem of overlapping orders, but the spectral dispersion varies greatly over the wavelength range of interest.

The straightforward approach of using dichroic beamsplitters followed by bandpass filters, e.g., such as used on the Pioneer 10 and 11 IPPs, is another possibility. This approach is simplified if the number of spectral bands to be isolated is limited. Since the signal-to-noise performance can be achieved with a very small telescope aperture of approximately 1-cm diameter, the use of dichroic beamsplitters combined with a multiple telescope approach has been selected as the best method for achieving the high-quality data required to meet the science goals with a high-reliability, relatively low-cost instrument.

Scan Method. A dual-mirror, object-space scan mirror system will be used for EOSP. A single-mirror scanning system was rejected since significant instrumental polarization would be introduced. This instrumental polarization would result because the reflectances of the parallel (P) and perpendicular (S or senkrecht) components of the beam with respect to the plane of incidence at the mirror differ when used at a non-normal angle of incidence; i.e., it acts as a partial polarizer . This is illustrated in Figure 9 for a representative protected silver design (100 nm Ag plus 30 nm Al_2O_3 plus 113 nm SiO_2) used at a 45° angle of incidence. Also indicated is the effect on the mirror polarization, P(t), resulting from the addition of various thicknesses of a contaminant of thickness t (in nm) with the contaminant having optical constants of n=1.5 and k=0.

In addition, the P and S components experience a different phase shift upon reflection, resulting in a net retardance due to the non-normal angle of incidence. However, when two identical mirrors are arranged such that both the angle of incidence on each is at 45° for all scan angles and the P plane of one mirror is the S plane of the other, then the polarization characteristics of the incident flux is unaltered by such a dual-mirror system.

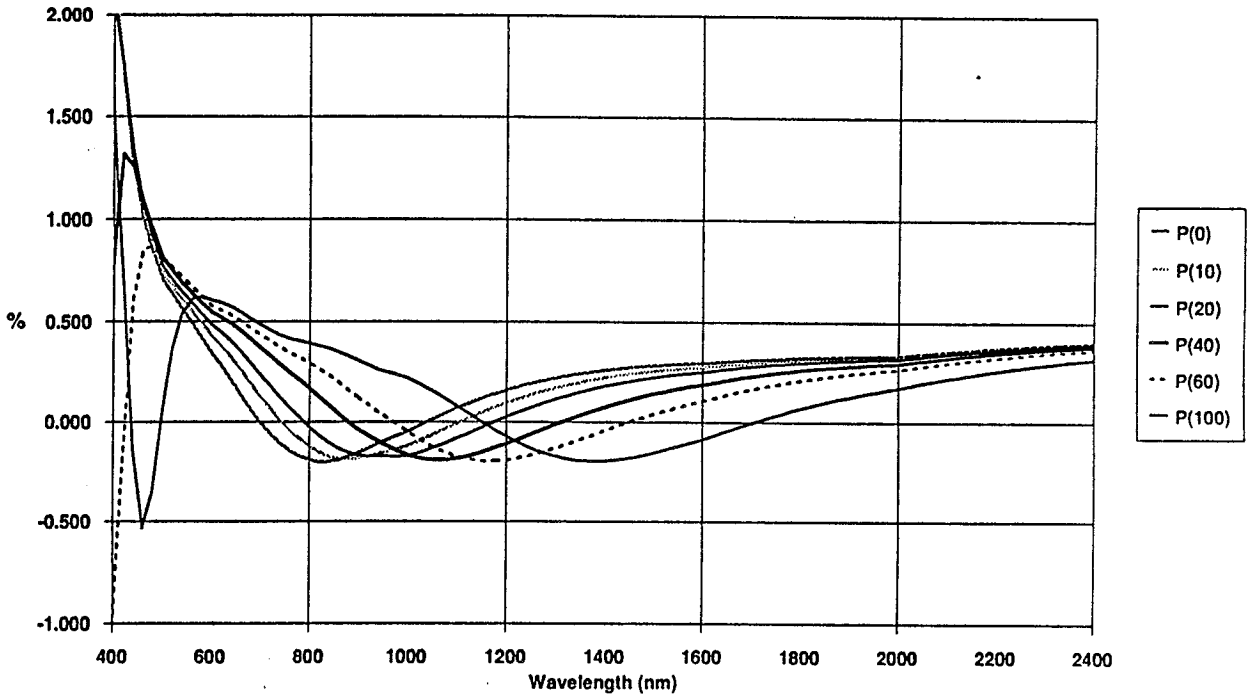

Figure 9. Polarization, P(t), from a protected silver mirror at 45° angle of incidence for various contaminant layers of thickness, t (in nm).

Any differences between the mirror reflectances of the two scan mirror elements will introduce some instrumental polarization. However, by coating both mirrors in the same deposition run, such differences can be minimized. Furthermore, since the scan mirror configuration selected has the same angle of incidence (45°) for all scan angles, any instrumental polarization will be constant with scan angle, thus simplifying both ground and inflight determination (calibration) of this important characteristic. The quantity,

$$P(t_1,t_2)=\{R_S(t_1)R_P(t_2) - R_P(t_1)R_S(t_2)\}/\{R_S(t_1)R_P(t_2)+R_P(t_1)R_S(t_2)\}$$

provides a measure of such differences in the case where the mirror reflectances, R, for the S and P polarization planes (indicated by subscript) are altered by contaminant coatings of thicknesses t_1 and t_2 (in nm) on mirrors 1 and 2, respectively. Figure 10 illustrates the resulting net

polarization for several coating thicknesses and differences. The optical properties of the contaminant films again are assumed to be n=1.5 and k=0. Note that P(t,t) for identical coating thicknesses is always zero, indicating the importance of ensuring that any contamination of the mirrors is equalized. It is apparent that with increasing contaminant layer thicknesses, there is less tolerance to contaminant mismatching on the two mirrors. From this analysis, a molecular contaminant allocation ($t_1 \leq 20$ nm and $|t_1 - t_2| \leq 2$ nm) of Level B (per MIL-STD-1246) can be established which can be met with reasonable controls during assembly, testing, launch, and on-orbit operations. Furthermore, to enhance control (minimization) of both the absolute and differential contamination, the scan mirror assembly is enclosed with fused silica windows at the entrance and exit ports.

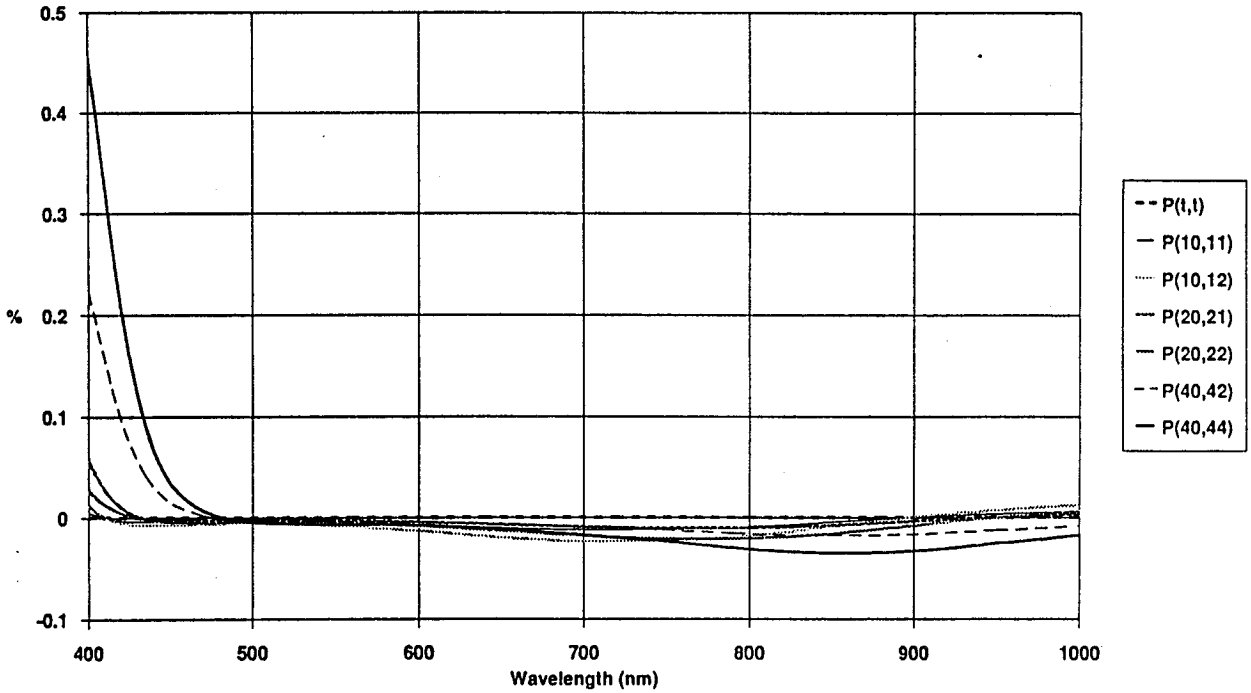

Figure 10. $P(t_1,t_2)$ versus wavelength for various contaminant thicknesses with t_1 for mirror #1 and t_2 for mirror #2.

A protected silver coating such as that used successfully on the Landsat Multispectral Scanner and Thematic Mapper sensors will be used for the two scan mirrors. This coating choice is best from the throughput and polarization viewpoints for the EOSP spectral range. The selected dual-mirror scan method requires that two mirrors be rotated in tandem to provide the scan, rather than the more usual motion of one mirror. The very modest spatial resolution requirements needed for the EOSP together with the relatively small total aperture needed—even for the eight boresighted telescopes—allows the dual-mirror scan system to be fabricated as a

light weight, low moment of inertia assembly. The continuous rotation approach selected for the EOSP scanning further simplifies the drive requirements and reduces the stiffness requirements for the assembly.

Telescope and Relay Optics. Refractive optics are used in the EOSP telescope and relay optics to simplify packaging and reduce size and mass. Additionally, the refractive optics can result in lower instrumental polarization than reflective designs. Figure 11 illustrates the schematic layout of the telescope assembly and the relative locations of the various elements. With the exception of the polarization and spectral filtering elements, either fused silica (Schlieren-grade) or radiation-resistant crystalline materials will be used. In the telescope fore-optics these materials will be combined to form an air-spaced achromatic doublet to cover the EOSP spectral range with greatly reduced chromatic aberration. This is necessary to obtain the same scene footprint at all wavelengths. Thus, the desired correction is to have the same focal length at the three separate wavelengths of each telescope, i.e., an apochromatic design as opposed to a classical achromat in which the correction is attained at the extremes of the spectral range, with a residual error ("secondary spectrum") at some intermediate wavelength. The selected design yields an image blur of about 21 μm that is considered quite acceptable (as compared to the 710 μm field stop diameter). The high index element of each telescope objective lens will be anti-reflection (AR) coated with single layers of MgF_2 on each surface, with different coating thicknesses on the two surfaces to optimize the bands approximately equally. The low index element of each telescope objective lens is uncoated.

The relay lens preceding the Wollaston prism will serve to nearly collimate the beam prior to entering the prism. These fused silica lenses will be uncoated. The focusing lenses are AR coated at the band wavelength to reduce cross-talk between orthogonal polarizations and increase channel transmittance. For each VINIR band a focusing lens in combination with the relay lens reimages the field stop onto the two silicon photodiodes. For each SWIR band similar optics plus a field lens at each detector results in the aperture being imaged onto the two HgCdTe detectors.

Wollaston Prism. For the EOSP application, a Wollaston prism deviation of a few degrees is adequate to provide the required spatial separation of the orthogonally-polarized components. A cell-mounted, two-element Wollaston prism fabricated of calcite is suitable for the spectral range spanned by the EOSP. It provides an extremely high extinction ratio (near 10^5) for near ideal polarization separation. The small separation angle (less than 4°) coupled with the large birefringence of calcite minimizes aberrations. The two elements are bonded together and then bonded into an aluminum cell using a high-purity, low outgassing silicone elastomer. With this technique developed for use on the IPP and subsequently used on the CPP and PPR instruments,

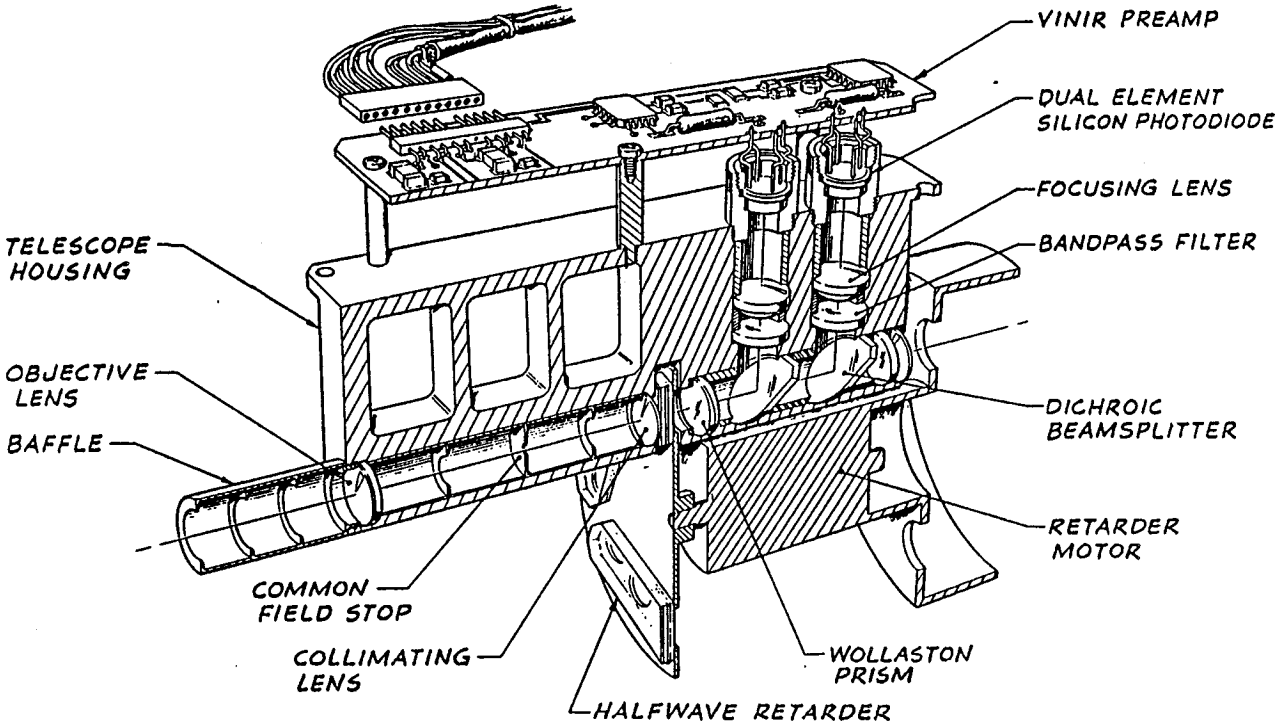

Figure 11. Schematic of modular EOSP telescope assembly.

the Wollaston prism assembly can be temperature cycled over a -40 to +50°C temperature range (which would fracture a rigidly-bonded calcite Wollaston prism due to a large thermal expansion mismatch of the bonded anisotropic prism elements). The calcite material will be screened for radiation damage in a manner similar to that used on the Pioneer and Galileo missions to Jupiter (Pellicori et al., Appl. Opt. 18, 2618, 1979) to preclude the possibility of radiation darkening or fluorescence due to impurities in the calcite material. The Wollaston prism outer surfaces are uncoated.

Halfwave Retarder. Each halfwave retarder must function over the three spectral bands serviced by each EOSP telescope and therefore must be suitably achromatized. A retarder fabricated with two different birefringent materials (Clarke, Optica Acta 14, 343, 1967; Beckers, Appl. Opt. 10, 973, 1971) is one method for extending the spectral range. This method of obtaining an achromatic halfwave retarder (AHWR) has been used on the CPP and the PPR where a positive ($n_e > n_o$) element (MgF_2 or crystal quartz depending on the spectral band) was combined with a negative ($n_o > n_e$) element (sapphire) to provide a significant increase of the angular acceptance of the combination. However, because the spectral range that must be covered by each halfwave retarder spans a factor of between 3.3 and 3.8, a different approach is required.

Another achromatization approach suggested by Pancharatnam (Indian Acad. Sci. A41, 137, 1955), involves an achromatic halfwave retarder formed from a combination of three

identical halfwave retarders, the first and third having their fast axes parallel and the second oriented at approximately 57°. The so-called super-achromatic halfwave retarders (Serkowski, p. 135 and Tinbergen, p.175 in *Planets, Stars and Nebulae Studied with Photopolarimetry*, ed. Gehrels, Univ. Arizona Press, 1971) combine three two-material AHWRs (in place of simple, single-material halfwave retarders) in the Pancharatnam configuration to achieve achromatization over an extended spectral range. The main disadvantage of this achromatic retarder is that there is wavelength dependence of the fast axis orientation as well as a wavelength dependence of the retardance. Another disadvantage is that a minimum of six individual elements are required in its construction. Beckers evaluated theoretically a number of two and three material combinations of which offered achromatization within about 5% over the 300 to 1100 nm range. However, the combinations cited all required very thin calcite, ADP or KDP elements of questionable practicality. For the EOSP application sapphire is used as one of the materials together with MgF_2 and crystal quartz, which allows element thicknesses to be determined that give exactly 180° retardance at three wavelengths. Since the three EOSP spectral bands serviced by each telescope pair are relatively narrow, this basic approach has been selected.

Each three-material EOSP AHWR is located in the collimated portion of the optical train to minimize retardance variation due to the angular range within the beam. Beckers (Appl. Opt. 11, 681, 1972) has suggested a method for increasing the angular aperture of a retarder by replacing one of the elements with two elements of the same material. These two elements are oriented with optical axes orthogonal, with a net thickness difference as previously determined for spectral achromatization, and with a total thickness as required to maximize the angular aperture. The EOSP AHWRs will use this technique and therefore consist of four individual retarder elements. The individual retarder elements will be bonded together using the same silicone elastomer used on the Wollaston prism to minimize multiple reflections between elements and to provide a low-stress coupling to eliminate any stress-induced birefringence due to thermal expansion mismatches between materials.

For the four-element EOSP designs there will be two sapphire elements in each AHWR. This allows the use of sapphire as the exterior elements of the combination to make it easier to achieve an efficient, broadband AR coating. This will minimize retardance errors due to multiple reflections with the EOSP AHWRs. Figure 12 shows the wavelength-dependent retardance for the retarder design optimized for the telescope pair which provides the 410 nm, 675 nm, and 1.25 μm spectral channels. In every case, as with this example, the retarder designs provide a deviation of no more than 1° from ideal 180° retardance (for an equally weighted average across the specified bandwidth of each band) at all three bands for a telescope pair.

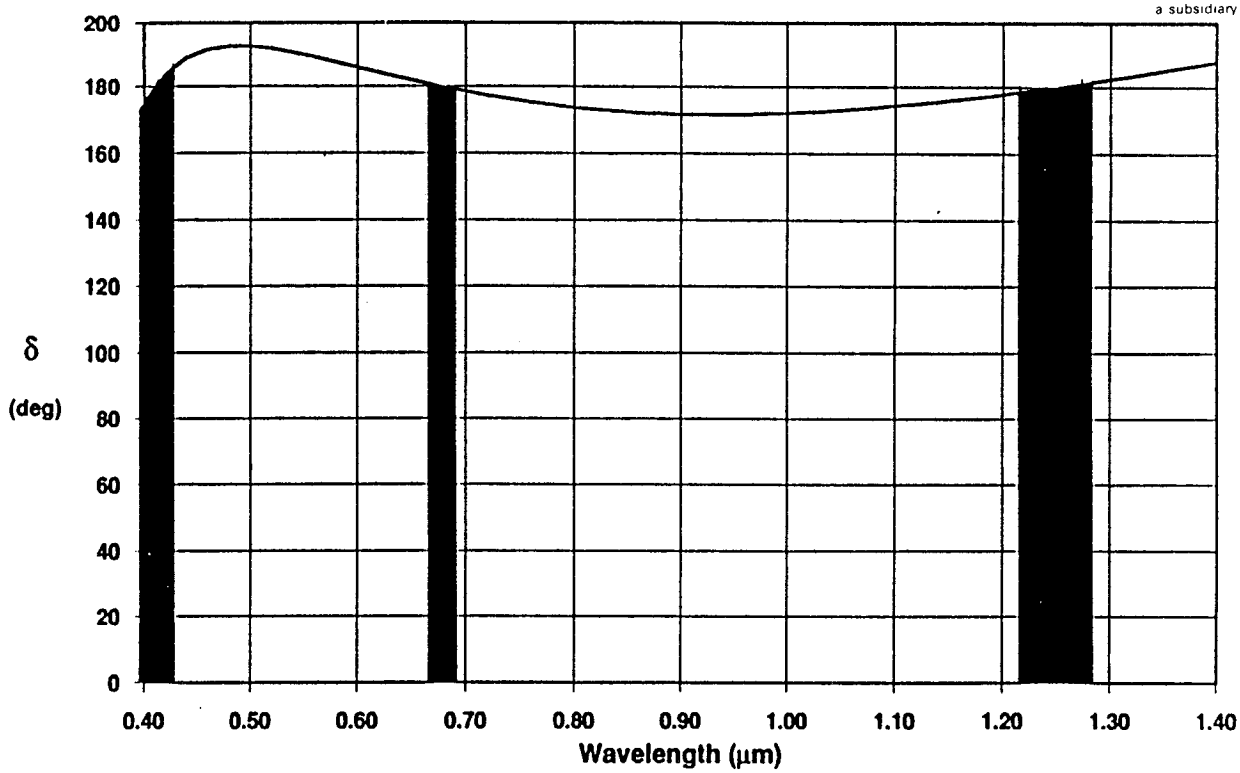

Figure 12. Retardance versus wavelength for halfwave retarder HWR12 servicing telescopes T1 and T2.

Spectral Filters. The definition of the required spectral bands will make use of dichroic beamsplitters together with bandpass filters. Following the polarization separation by the Wollaston prism for each telescope, two dichroic beamsplitters will provide the spatial separation of three wavelength regions (cf. Figure 11). As indicated in Table 2, the shortest wavelength region is reflected by the first dichroic beamsplitter (essentially with reflectance equal to one minus the transmittance) with the longer wavelengths being transmitted. The azimuthal orientation of the P-plane of the dichroic beamsplitter is chosen at 45° to the plane of deviation of the Wollaston prism to minimize any spectral shaping differences for the two orthogonally polarized beams. The separation at the second dichroic beamsplitter is analogous to that at the first, with the shorter wavelengths again reflected and the longer wavelengths transmitted. One pair of dichroic beamsplitters will be used in one group of four telescopes, with second pair being used in the other group of four, as illustrated schematically in Figure 13. Non-optimized designs for the dichroic beamsplitters A2 and B2 are shown in Figure 14, illustrating that the required separations for the two groups of three EOSP bands are easily provided.

In the EOSP optical design the bandpass filter is located prior to the focusing lens, rather than in the converging beam following the lens. In this location, angle of incidence effects are negligible, since the total angular range is less than 5°. The high out-of-band rejection filters will

Table 2. EOSP Telescope and Dichroic Beamsplitter Configuration

Band	Telescopes	Dichroic Beamsplitters
410 nm	T1 & T2	A1(R)
470 nm	T3 & T4	A1(R)
555 nm	T5 & T6	A2(R)
615 nm	T7 & T8	A2(R)
675 nm	T1 & T2	A1(T) + B1(R)
750 nm	T3 & T4	A1(T) + B1(R)
880 nm	T5 & T6	A2(T) + B2(R)
950 nm	T7 & T8	A2(T) + B2(R)
1.25 μm	T1 & T2	A1(T) + B1(T)
1.60 μm	T3 & T4	A1(T) + B1(T)
2.05 μm	T5 & T6	A2(T) + B2(T)
2.25 μm	T7 & T8	A2(T) + B2(T)

General notes:

1. Telescopes T1, T3, T5 and T7 have the Wollaston prism oriented for measurement at the 0° and 90° polarization azimuths while T2, T4, T6 and T8 make measurements at 45° and 135°.
2. During inflight polarimetric calibrations the roles of the detectors used for the 0° and 90° (and similarly for 45° and 135°) measurements are interchanged when the halfwave retarder for each telescope pair, e.g., T1 and T2, is rotated 45°. The roles of the 0°/90° and 45°/135° telescopes are interchanged when the halfwave retarder is rotated by 22.5°.
3. The letter designation of the dichroic beamsplitter indicates whether the flux is reflected (R) or transmitted (T) for the associated band.
4. Bandpass filters are used to define the spectral passband following dichroic splitting.

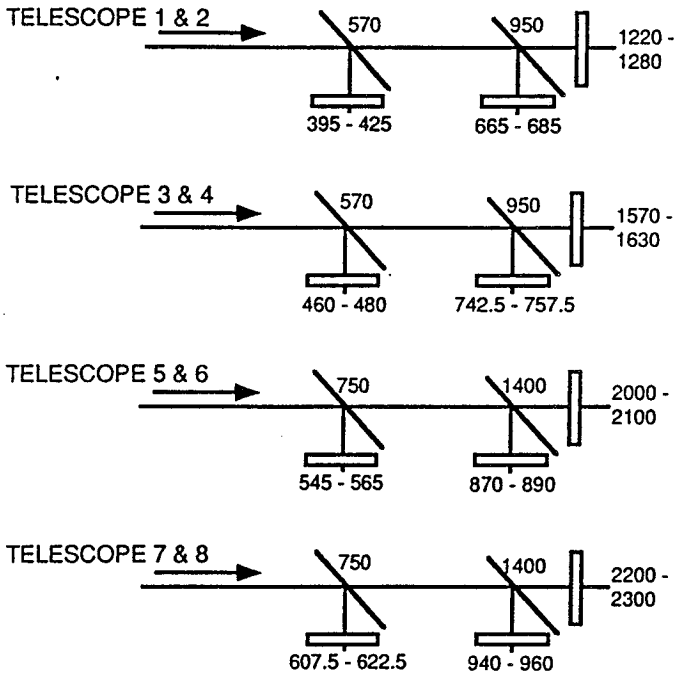

Figure 13. Spectral definition by telescope with the dichroic beamsplitter and bandpass filter wavelengths indicated in nm.

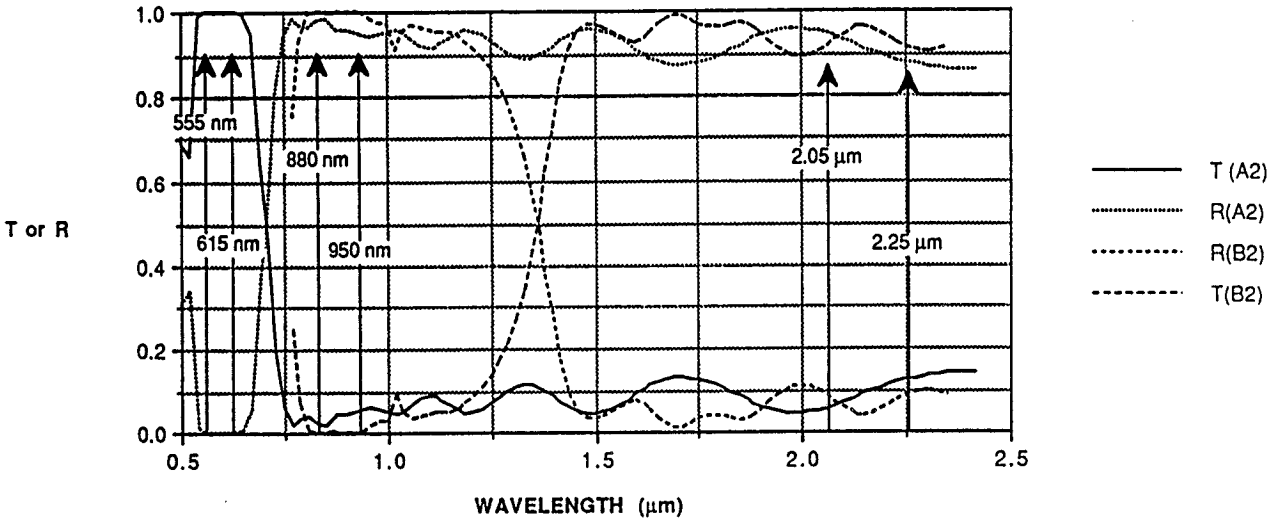

Figure 14. Transmittance or reflectance for the dichroic beamsplitters A2 and B2 (see Table 2).

be similar to those used on the CPP and PPR and are well within the state of the art. Materials for the spectral filter substrates and coatings will be restricted to those known to be adequate for the expected radiation environment.

Detectors. The detectors for the VINIR bands will be blue-enhanced silicon photodiodes. Since the spectral response of such photodiodes is adequate for our requirements at the longest VINIR bands of interest, it is planned that all VINIR detectors be identical. The dual-element silicon photodiodes (0.75-mm diameter detectors with a center to center spacing of 1.5 mm) are mounted in a TO-5 package. The detectors are operated at zero bias with high shunt resistance so that electronics noise is dominated by the 50-Mohm feedback resistor. A machinable tungsten housing for the detector package provides more than adequate radiation shielding. AR-coated Schott GG375G34 radiation-resistant glass will be used as windows on these assemblies.

The SWIR spectral bands will use photovoltaic HgCdTe detectors selected for their excellent performance with relatively modest cooling. Two HgCdTe detector pairs will be located on each of four quadrant substrates which in turn are mounted on an aluminum nitride motherboard. The motherboard, which also contains the cold focal plane (CFP) temperature control sensor and heater, is bonded to the thermal-isolating titanium stem of the CFP assembly. This is illustrated in Figure 15, which also indicates the method for routing electrical signals via four flexible cables and the method for heat transfer coupling to the simple, single-stage radiation cooler.

Mounted within the vacuum enclosure (not shown) are ambient temperature windows that separate the CFP from the ambient temperature optics. The detectors will be of the planar, ion-implanted, n+ collector on a p-type base configuration. In this approach (Kosai et al., Proc. IRIS Detector Specialty Group, 1985), the p-type base in HgCdTe is grown on a CdZnTe substrate by means of liquid phase epitaxy (LPE). In this structure the detectors are illuminated from the back side, through the CdZnTe substrate, which is transparent to the infrared wavelengths of interest. This configuration is chosen because it takes advantage of high-quality LPE HgCdTe grown on relatively large CdZnTe substrates. The decreased defect density of the LPE-grown HgCdTe permits large area diodes with good uniformity and high R_0A_j (the product of the zero-bias dynamic resistance, R_0, and the detector junction area, A_j). Moreover, backside illumination increases quantum efficiency and reduces the possibility of interference effects from the passivation layer, which can cause undesirable variations in spectral responsivity characteristics.

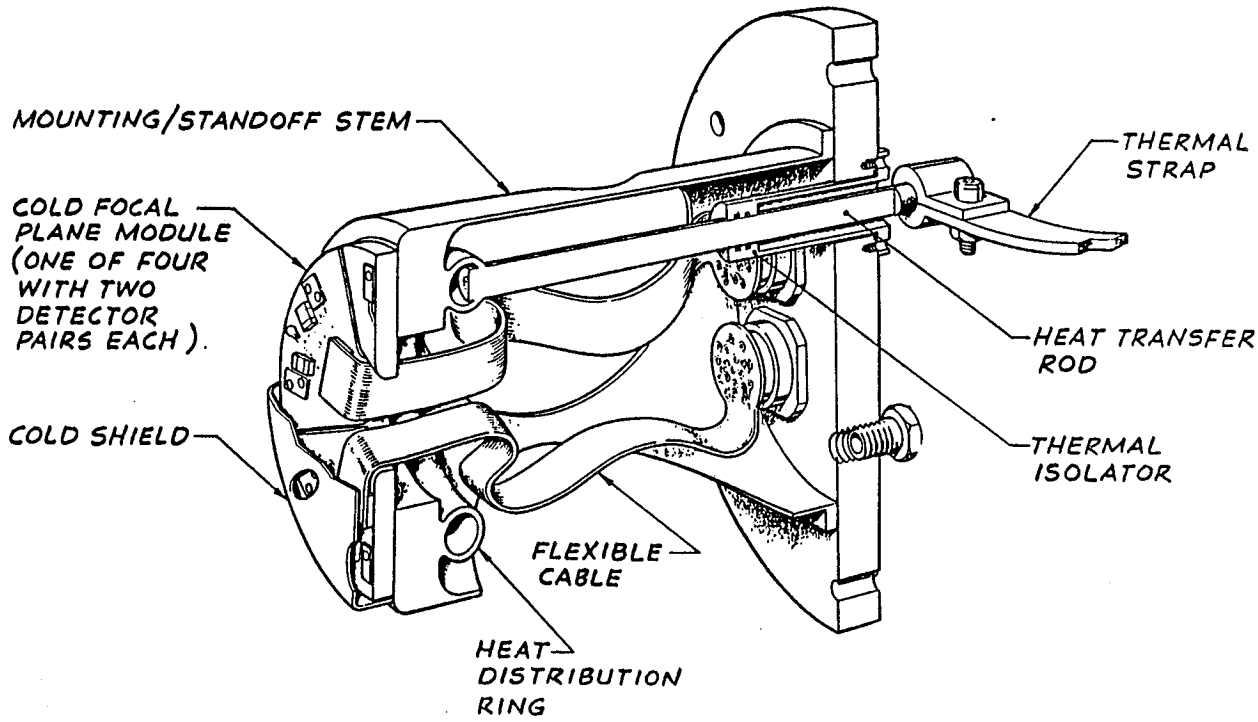

Figure 15. Schematic representation of the cold focal plane assembly.

As discussed in the next section (Performance), R_0 has a significant effect on the signal-to-noise performance, leading to the choice of an operating temperature of 185K for the 2.5 μm cut-off detectors suitable for the EOSP SWIR bands. Figure 16 shows typical R_0A_j versus temperature data for detectors with three different cut-off wavelengths. For the 0.35-mm diameter detectors that can easily be accommodated by the EOSP optical design, an R_0 of 12 Mohm can

be expected when the focal plane is controlled to an operating temperature of 185K. The quantum efficiency can be expected to be flat with values between 60 and 70% over the EOSP SWIR spectral range.

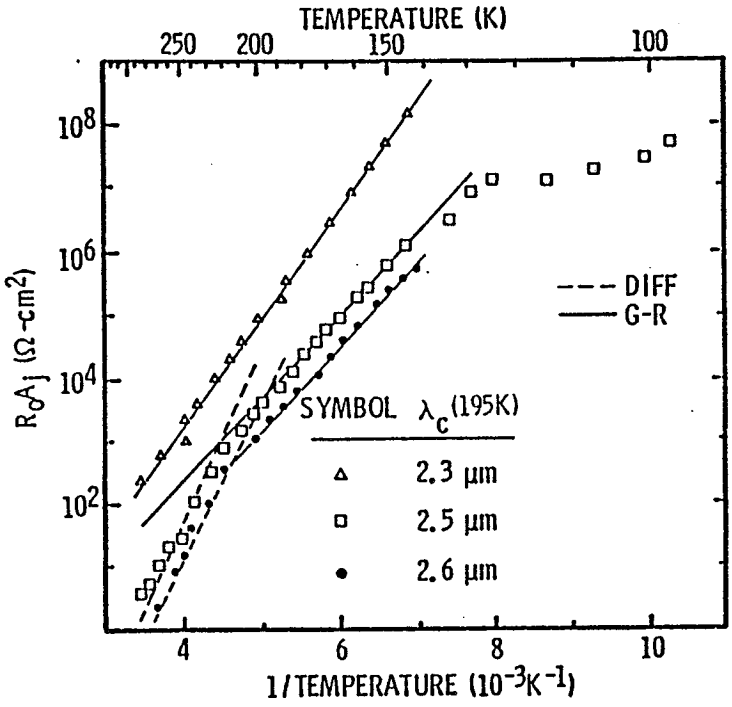

Figure 16. Product of the zero-bias dynamic resistance and the detector junction area, R_0A_j, as a function of temperature for detectors with the three indicated cut-off wavelengths.

Contamination Protection and Control. There are three primary environments associated with the instrument life where contamination control must be considered for the EOSP; i.e., (1) the pre-launch period, (2) the launch, and (3) normal inflight operations. During the pre-launch instrument phase, the normal care usually imposed on spaceflight instruments are expected to adequately protect the instrument, i.e., a clean room/flow bench environment with the instrument being handled only by trained personnel wearing gloves. During both the launch period and the inflight servicing periods it is planned that the scan mirror assembly be positioned in the "stow" position; i.e., with the scan mirror assembly oriented to view the instrument housing to provide substantial protection of the optics. During the normal inflight portion of the mission, it is not anticipated that any precautions will be required except possibly to delay first usage of the instrument following launch until any "contamination cloud" has dissipated sufficiently. The critical scan mirror assembly is protected by fused silica entrance and exit windows to minimize the

risk of asymmetric contamination of the two mirrors. The radiation cooler will be covered during launch with a lightweight cover that will serve as an earth shield when unlatched.

2.4 PERFORMANCE

The signal-to-noise ratio (SNR) is specified to be >2000 for each EOSP channel when viewing a solar illuminated scene at 1 AU (earth orbit) with a geometric albedo of 0.3. The scene spectral radiance, $L(\lambda)$, at wavelength λ is given by

$$L(\lambda) = p(\lambda)\, H_e(\lambda)/\pi$$

where $p(\lambda)$ is the spectral geometric albedo, and $H_e(\lambda)$ is the solar spectral irradiance at 1 AU. The number of signal electrons, S_{scene}, generated during an integration time, T_{int}, by a detector is

$$S_{scene} = T_{int}\, A_o\, \Omega_o \int T_o(\lambda) L(\lambda)\, \eta(\lambda)\, (\lambda/hc)\, d\lambda$$

where:

A_o = Effective aperture area (cm^2);
Ω_o = Solid angle of IFOV (sr);
$T_o(\lambda)$ = Optical system transmittance at wavelength λ;
$\eta(\lambda)$ = Quantum efficiency at wavelength λ (electrons/photon);
h = Planck constant = 6.62×10^{-34} W sec^2; and
c = Speed of light = 2.998×10^{17} nm/sec.

The narrow spectral bandwidths of the EOSP bands permit the use of mean values for the spectrally dependent variables, leading to the simplified form for the signal as

$$S_{scene} = T_i\, A_o\, \Omega_o\, T_o(\lambda)\, L(\lambda)\, \Delta\lambda\, \eta(\lambda)\, (\lambda/hc)$$

where λ is the center wavelength of the spectral bandpass, and $\Delta\lambda$ is the spectral bandwidth.

The total noise associated with the detection process is the root sum square (rss) value of the instrument noise sources. For EOSP, the primary noise sources are scene shot noise (N_{shot}), detector-generated noise (N_{det}), amplifier noise (N_{amp}), and quantization noise (N_{quant}). Thus, the SNR is given by

$$SNR = \frac{S_{scene}}{\sqrt{\{N_{shot}^2 + N_{det}^2 + N_{amp}^2 + N_{quant}^2\}}}.$$

N_{shot} includes contributions from both the scene signal electrons and from the background-generated signal electrons, with the noise being equal to the square root of the sum of these signal plus background electrons, i.e.,

$$N_{shot} = \sqrt{(S_{scene} + S_{bkgd})}.$$

For EOSP, the background-generated electrons are negligible for the silicon photodiodes used for the VINIR bands as well as for the 2.5-μm cutoff wavelength HgCdTe photodiodes used for the SWIR bands. N_{det} for the silicon photodiodes is negligible since the detector shunt resistance is expected to be greater than 2000 MΩ at 30°C, and the leakage current will be negligible due to operation near zero bias. In contrast, the thermal noise associated with the detector resistance of the HgCdTe photodiodes will be the dominant noise for the EOSP SWIR channels. Thus, for the EOSP SWIR channels, the detector noise is approximated well by

$$N_{det} = \sqrt{\{2\,k\,T_{det}T_{int}/R_d(T_{oper},V_{bias})\}} \,/\, e$$

where:

k = Boltzmann constant = 1.38×10^{-23}(W/sec/K);
T = Absolute temperature (K);
$R_d(T_{oper},V_{bias})$ = Detector resistance (ohm) at T_{oper} and V_{bias}; and
e = Electronic charge = 1.60×10^{-19} coulomb.

N_{amp} is dominated by the thermal noise of the feedback resistor for the frequency bandwidth needed and for the feedback resistor values selected for EOSP as discussed in the Electronics section. For the EOSP where the low pass filter bandwidth is less than 200 Hz, the preamplifier input noise current and voltage contributions are negligible. Thus,

$$N_{amp} = \sqrt{\{2\,k\,T_{fb}T_{int}/R_f\}} \,/\, e.$$

In the above noise equations it is implicitly assumed that the noise bandwidth, Δf_n, is equal to that of a true integrator, i.e., $(2T_{int})^{-1}$. However, the use of dc-restoration will reduce the noise bandwidth, while the presence of boosted amplifier voltage noise or 1/f noise components will increase the effective noise bandwidth. For the EOSP instrument, these effects are small enough to be ignored. Finally, N_{quant} is given by

$$N_{quant} = S_{fs}/(2^N \sqrt{12})$$

where S_{fs} is the full-scale signal (in electrons) and N is the number of quantization bits.

Silicon photodiodes suitable for the EOSP are available with zero bias resistances exceeding 2000 Mohm at 25°C for sizes up to 2-mm diameter, thus allowing the use of 50 Mohm feedback resistors for the EOSP VINIR channels. This will result in the signal shot noise exceeding thermal noise of the feedback resistors in all VINIR channels for p=0.3 with the modest telescope aperture of 1 cm selected. Furthermore, since these detectors will be operated virtually at zero bias, the dark current noise will be negligible for the EOSP VINIR channels.

The situation for HgCdTe detectors is different, since cooling of the 2.5-mm cutoff detectors suitable for the EOSP SWIR requirements is required to achieve a sufficiently high R_0A_j for a similar signal shot noise to feedback resistor noise condition. Cooling these SWIR detectors and preamplifiers has the combined effect of allowing a larger feedback resistor and reducing the associated thermal noise due to the lower temperature. As discussed in the Mechanics section, a simple single-stage radiative cooler can provide cooling to 175K. Even with the CFP controlled to 185K (one of the eight selectable control temperatures), the performance of the SWIR channels meets the criterion of a minimum signal-to-noise ratio of 2000 (to obtain 0.1% polarimetry for scenes of low polarization) when p=0.3. Table 3 summarizes the expected SNR performance for the EOSP instrument for the nominal condition with p=0.3 as well as for p=0.1 and 1.0.

2.5 MECHANICAL DESIGN

The mechanical design of the EOSP emphasizes the use of proven techniques and mechanisms to provide a high reliability instrument. The modular design described will allow the complete testing of individual subassemblies prior to final assembly and facilitate the use of simplified final assembly techniques, while assuring that the required final optical alignments are achieved. The key mechanical subsystems are: (1) scan mirror assembly and drive, (2) structural frame, (3) telescopes, (4) cold focal plane, (5) electronics module, (6) halfwave retarder wheel and drive, (7) calibrator, (8) solar diffuser, and (9) thermal control.

Scan Mirror Assembly and Drive. The protected-silver-coated, twin scan mirrors will be mounted in a carrying tube with entrance and exit apertures sealed by fused silica protective windows (see Figure 17). The tube will be brazed to a ring which acts as a light and debris shield. An entrance baffle joins the ring to the tube and prevents unwanted light from scattering around this assembly. The carrying tube has a mounting flange used to anchor to the low profile scan motor. A tradeoff between low mass, low inertia and the ability of the scan motor to provide smooth motion was made. The relatively slow speed (40.5 rpm) of the motor and a potentially low inertia of the tube/mirror/window subassembly can challenge the designer to deliver smooth scanning motion. A relatively higher inertia of this subassembly will reduce cogging and ripple effects during scanning. A weight penalty is accordingly accepted in using an aluminum

Table 3. EOSP Performance Summary

λ (nm)	Δλ (nm)	To	η(λ)	L(λ) for p=0.3 W/(cm2-sr-nm)	Sscene (e)	Nshot (e)	Ndet (e)	Namp (e)	Nquant (e)	Ntotal (e)	SNR (p=0.3)	SNR (p=1.0)	SNR (p=0.1)
Si Pd					p=0.3								
410	30	0.120	0.46	1.585E-05	2.226E+07	4718	731	4620	1961	6927	3213	6298	1361
470	20	0.149	0.66	1.900E-05	3.633E+07	6027	731	4620	3201	8274	4391	7557	2043
555	20	0.150	0.74	1.757E-05	4.477E+07	6691	731	4620	3944	9067	4938	8047	2404
615	15	0.150	0.75	1.633E-05	3.505E+07	5920	731	4620	3088	8152	4299	7469	1985
675	20	0.135	0.77	1.451E-05	4.213E+07	6490	731	4620	3711	8819	4777	7908	2295
750	15	0.142	0.74	1.213E-05	2.965E+07	5445	731	4620	2612	7639	3881	7050	1733
880	20	0.142	0.66	8.938E-06	3.049E+07	5522	731	4620	2686	7719	3950	7121	1773
950	20	0.137	0.64	7.773E-06	2.678E+07	5175	731	4620	2359	7364	3637	6787	1592
HgCdTe													
1250	60	0.123	0.65	4.269E-06	5.293E+07	7276	7406	4684	4663	12307	4301	7932	1793
1600	60	0.131	0.65	2.387E-06	4.036E+07	6353	7406	4684	3556	11393	3543	7173	1405
2050	100	0.118	0.65	1.012E-06	3.292E+07	5737	7406	4684	2900	10868	3029	6558	1165
2250	100	0.093	0.65	7.248E-07	2.039E+07	4515	7406	4684	1796	10020	2035	5057	742

Parameters used: Tint=3.3msec; Ao=0.785 cm2 (Dtel=1cm dia.); Ω=1.58E-4sr (IFOV=14.2mr dia.); Adet=9.6E-4cm2 (Ddet=0.35mm dia.); solar spectral irradiance values from Labs, D. and Neckel, H. Solar Phys. 15, 79 (1970) and Proc. of Symp. on Solar Radiation, Smithsonian Institute, Washington, D. C., 269 (1973) used to compute L(λ) values; Rdet=2000Mohm, Tdet=300K, Rf=50Mohm, Tfb=300K used for VINIR (SiPd) channels; Rdet=12Mohm, Tdet=185K, Rf=30Mohm, Tfb=185K used for SWIR (PV HgCdTe) channels; and 14-bit quatntization with full scale signal assumed for p=1.5.

structure and glass mirror substrates in lieu of the lighter but more costly and difficult to handle materials such as magnesium and/or beryllium. A latching mechanism will be used to cage the tube assembly for the launch and initial platform deployment. Following initial deployment, the scan mirror assembly can be stowed by command such that the aperture of the tube assembly is driven to an encoder-defined position beyond the scene-viewing slot in large outer housing. That outer housing also has an aperture on the side opposite the scene-viewing slot for viewing the polarization calibrator (cf. Figure 17).

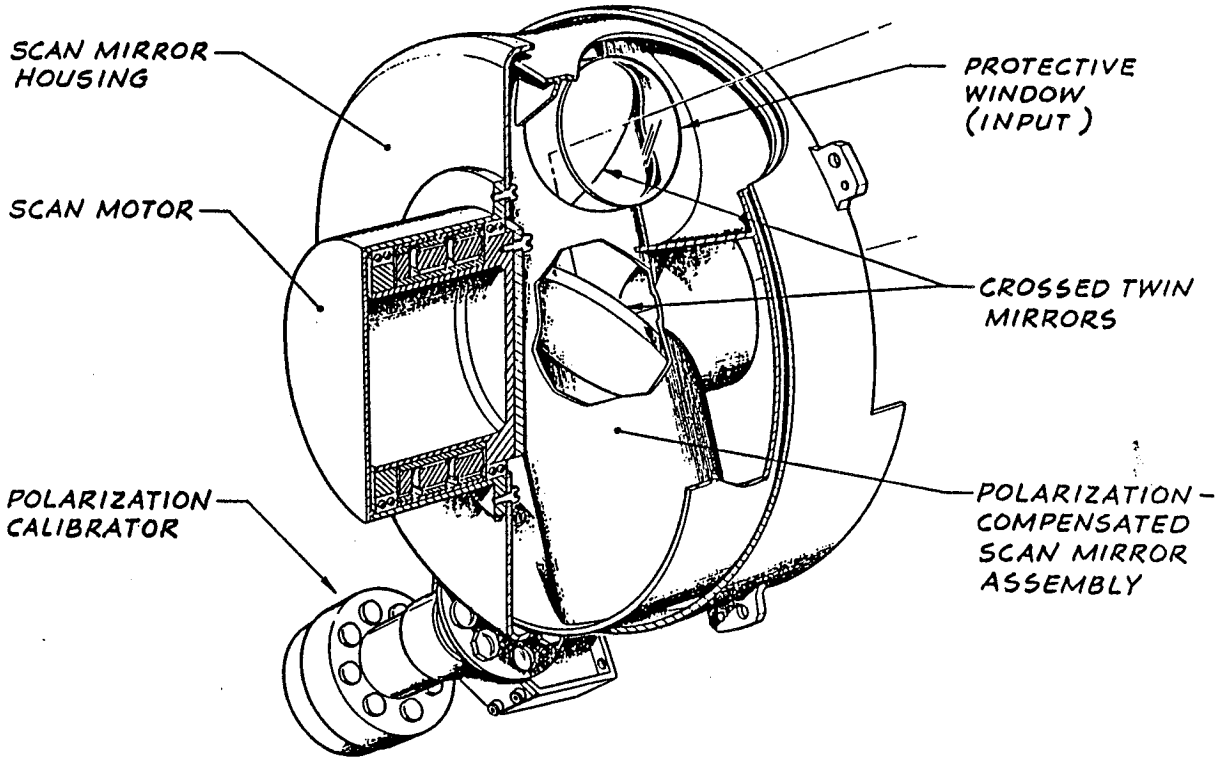

Figure 17. Schematic representation of twin scan mirror assembly, housing, scan motor, and polarization calibrator.

The drive mechanism for the scan mirror assembly will have redundant windings and will be counterbalanced and supported by a pair of bearings. The mirror set will rotate continuously in one direction at 40.5 rpm and have a mass moment of inertia about the rotation axis of approximately 50 kg cm^2. Long-term reliability of this rotating mechanism will be achieved by using anti-friction ball bearings with special lubricants applied to the balls and races. Bearing geometries and lubrication materials will be selected to ensure operation in the elastohydrodynamic region as opposed to the boundary lubrication region. The EOSP five year life at 100% duty cycle will demand a 107 million cycle operational and test life for the scan mirror drive. This is well within the current proven technology of lubrication. Ion plated lead has performed

well as a lubricant on the Giotto Mission and used with Braycoat 815Z oil has proved successful at 250 million cycles on a Landsat sensor. Recent work indicates that a combination of ceramic balls and Braycoat 815Z may eliminate the problem of polymerization. The scan assembly is caged at launch and released by means of a latch mechanism using two (the second for redundancy for this critical function) wax pellet actuators controlled by relay commands. Upon receipt of the scan mirror latch release command, the actuator releases the caging pin and locks it in the released position. The latch mechanism can released/reset manually.

Structural Frame. The scan (forward) bulkhead, cold focal plane (rear) bulkhead, telescope mount, and the electronics baseplate bolt together to form the structural skeleton of the EOSP (cf. Figure 6). The scan bulkhead carries the scan drive assembly and the polarization calibrator. Alignment testing will establish accurate positioning and final drilling/pinning will facilitate disassembly and reassembly. A cutaway allows access to power and signal connectors between the electronics module and the scan motor, latch actuators, and encoders. The rear bulkhead carries the preamplifier boards for the cold focal plane. The telescope mount rests on two pads at each bulkhead. This octagonal mount provides the registration surfaces for the eight telescopes. It will be machined to allow positional adjustments and shimming for each individual telescope. Alignment testing and subsequent selection of shims will ensure that the telescopes are properly aimed at the scan mirror assembly. The CFP end of the octagonal structure will be sealed with windows to create a vacuum chamber for ground cold testing of the CFP. Low emissivity gold plating in the chamber area minimizes heat transfer by radiation to the CFP. Instrument thermal control will maintain the structural portion of the instrument at $20° \pm 20°C$ during operation, thereby allowing the use of common materials. Aluminum (6061-T6) has been selected for the structural components. The instrument will be attached to the platform payload mounting plate (PMP) via a 3-point mount (two at the forward bulkhead and one at the rear bulkhead) with thermal isolators between the mounting feet and the PMP.

Telescopes. Each of the eleven optical elements which make up an independent telescope will be fitted to an aluminum carrier. This carrier is created by a combination of electrical discharge machining and conventional milling operations. The element positioning and spacing is accomplished by the use of shims, gaskets, and metallic spacers. The dichroic elements have a geometry which enables them to be oriented properly. Optically black paint (e.g., Chemglaze Z-306) will be used to coat the baffles and interior tube walls. The preamplifier boards attach by means of standoffs. Each cable harness is routed forward to the bulkhead and down to the electronics module. Each telescope will be shimmed for alignment and then drilled/pinned for ease of disassembly/reassembly.

Cold Focal Plane. The key elements of the CFP are (1) four focal plane modules, (2) cold shield, (3) mounting stem, (4) heat transfer rod and distribution ring, (5) thermal isolator and strapping, (6) sealing cap, and (7) flexible fine line cables (see Figure 15). High conductivity aluminum nitride has been selected for the focal plane substrate. This material can be machined to have a generous radius for cable routing and electronic circuitry can be deposited directly to it. Each of the four modules can be thoroughly tested before integration with the mounting stem. The cold shield will reduce the heat load seen by the detectors. The mounting stem acts as a thermal insulator, yet must be structurally sound so as to prevent damage due to launch vibration. The present design employs titanium 6 A1-4V for the stem. A thin, relieved wall improves the thermal isolation. The stem will be gold plated to minimize radiative transfer. The heat transfer rod will be made of oxygen-free, highconductivity copper and joined to a distribution ring of the same material. This technique minimizes the temperature gradient directly below the focal plane modules. The rod will be insulated from the sealing cap by a delrin isolator.

A 500 cm^2 radiative cooler provides adequate cooling for on-orbit operation. The multi-layer thin foil copper cold strapping is to be attached to the radiator for space simulation testing and delivery of the instrument for payload integration. The strapping will be encased by a low emissivity cover. During ground testing, the cold strapping will be attached to a cold sink for cool down of the CFP. In practice, the ground cold test begins by attaching vacuum hardware to the sealing cap for a rough pump out. Cryo or sorption pumping will then allow the start of cool down without danger of icing the focal plane. Reusable O-rings seated in the thermal isolator and in the end of the octagonal structure are rated for 10^{-6} torr (a good insulating vacuum is 10^{-4} torr). The sealing cap has the bolt pattern for attachment to the octagonal structure, carries four connectors which join the CFP to the preamplifier boards, provides a vacuum sealing surface, receives the stem, and has a pump out and vacuum breaker port. This part can be aluminum because of the anticipated narrow operating temperature range. The four flexible fine line cables are similar in design to previously used, space-rated cables with twenty conductors 0.005 inch wide space on 0.015 inch centers. Standard wirebonding will be used to join gold wires from the focal plane modules to the cables. Essential design features include strain relief, a service loop permitting connector attachment, and a transition from rectangular cable to round connector.

Electronics Module (mechanical aspects). An interconnecting scheme was carefully selected after review of possible approaches. The five frames will connect internally and present external connectors for routing to the Eos platform interface, test equipment, motors and encoders, and focal planes. An all external approach appeared excessively complicated, required more physical space, and had a significant mass penalty. The internal connections between frames requires a rigid structure and accurate alignment pins to prevent pin or socket damage

during blind insertion. This approach has been used successfully for instruments on a number of missions including the predecessor CPP and PPR instruments. A cover with MLI blanketing will enclose all but the spacecraft interface and test connectors on the inboard side. The cold space side of the electronics module will have 200 cm^2 of surface area coated with thermal paint for instrument cooling/thermal control.

Halfwave Retarder Wheel and Drive. The halfwave retarder wheel is positioned inside the octagonal telescope array so that each telescope is intersected by the wheel at a location between the collimating lens and the Wollaston prism (cf. Figure 11). The retarder wheel drive mechanism is a stepper motor of the same design used on the PPR instrument. It is positioned aft of the retarder wheel using a special mount within the octagonal structure and attached to the rear bulkhead by a fixture that surrounds the CPF assembly. An integral encoder provides the sensing/driving control for the motor. The moving portion of the retarder wheel assembly has a mass moment of inertia about its rotation axis of 0.4 kg cm^2. During repositioning of the halfwave retarder wheel, the peak angular velocity is about 4 radians/sec (11.25° in about 50 msec).

Calibrator. The polarization calibrator assembly is mounted on the forward bulkhead on the platform side of the outer housing for the scan mirror assembly (cf. Figures 6 and 17). Flux from the calibrator is directed through the 2.5-inch diameter cutout in the inner housing and is measured by the instrument when the view direction of the scan mirror assembly passes beyond the limb of the earth scene and coincides with the calibrator aperture location. The calibrator employs a wheel with eight optical element positions (one viewed by each of the eight EOSP telescopes). A calibration cycle involves measurements with each telescope viewing each of the eight wheel positions in turn, using a stepper motor identical to that employed for the retarder wheel. Alignment of the calibrator assembly will be achieved by optical testing and then maintained by drilling/pinning. As with the retarder wheel drive, an integral encoder provides sensing/driving control for the motor. Similarly, the moving portion of the retarder wheel assembly has a mass moment of inertia about its rotation axis of 0.4 kg cm^2. During repositioning of the polarization calibrator wheel, the peak angular velocity is about 4 radians/sec (11.25° in about 50 msec).

Solar Diffuser. A solar diffuser assembly is mounted on the top (nadir side) of the EOSP using a tripod fixture with two legs attached to the forward bulkhead and one to the rear bulkhead (cf. Figure 18). Upon command the diffuser element is deployed from its stow position into the scanned swath near the nadir direction using a bi-metallic, thermally-activated spring mechanism similar to that employed on the PPR for closing telescope covers. This thermal motor is "fail safe" in the sense that a failure of the heater element would result in loss of the solar diffuser view, but no loss of scene data. The moving portion of the solar diffuser assembly has a

mass moment of inertia of 5 kg cm^2 with a peak angular velocity of approximately 0.02 radians/sec. The diffuser is caged at launch and released by means of a latch mechanism using one wax pellet actuator controlled by relay commands. Receipt of a solar diffuser latch release command causes the caging pin to be retracted and allows the positioning of the diffuser element into the scanned swath of the instrument using the thermal motor. When the solar diffuser is not deployed for calibration measurements, the critical (reflective) surfaces are protected in the stow position from contamination and UV radiation.

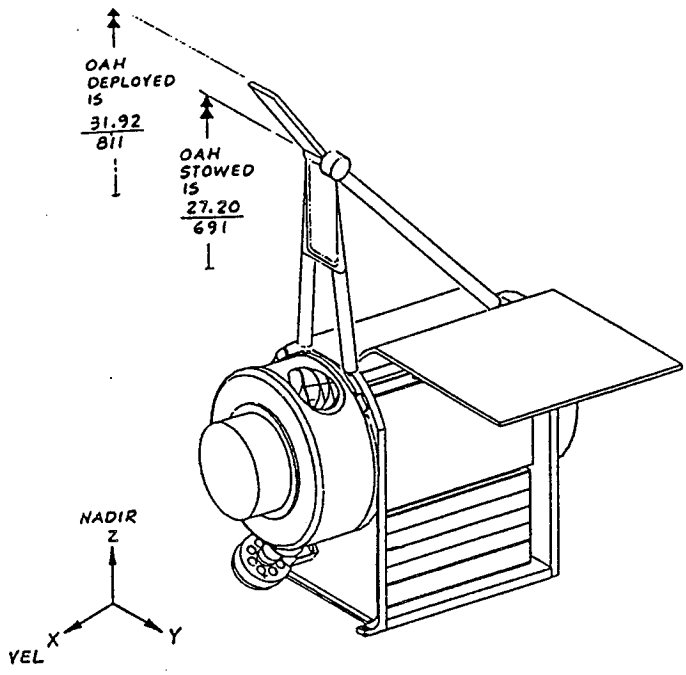

Figure 18. Schematic representation of solar diffuser assembly attached to the top (nadir side) of the EOSP.

Thermal Control. The cold focal plane is cooled by means of a single-stage radiative cooler. An earth shield with side skirts protects the radiator from earth thermal and albedo loads. Both structures are made of lightweight aluminum honeycomb and matching skin and are conductively isolated from the instrument. The earth side of the radiative cooler earth shield is painted white and the inner surface (viewable by the radiative cooler) is low emittance aluminum. The shield is spring loaded and initially held in place by a latching mechanism to thus serve as a contamination cover for the radiative cooler during launch (and after platform deployment until outgassing is minimal). Upon receipt of the earth shield latch release command, two (the second one for redundancy for this critical function) wax pellet actuators effect the retraction

of the caging pin and the resulting permanent deployment of the earth shield. The latch mechanism can be released/reset manually.

A performance assessment for the 500 cm^2 radiative cooler indicates that with the expected thermal loads, the cooler conservatively provides a CPF temperature of 170K. Satisfactory HgCdTe detector performance is expected up to 200K. Eight selectable (by command) temperature set points ranging from 170K to 200K are provided to accommodate for possible degradation of performance over the nominal five year life. The heat loads and temperature estimates are summarized in Table 4.

Table 4. Heat Load and Temperature Estimates for EOSP Radiative Cooler

Heat Load Source	Heat Load (W)
Detector/Preamp Joule Heating	0.020
Flat Cables (4)	
Conduction	0.003
Radiation	0.160
Optical Window (8) Radiation	0.066
Titanium Support/Isolator	
Conduction	0.202
Radiation	0.295
Delrin Seal/Isolator	
Conduction	0.006
Radiation	0.013
Heat Transfer Rod (OFHC) Radiation	0.044
Thermal Strap Radiation	0.150
Radiator Rear Surface Radiation	0.380
Radiator Supports/Isolators Conduction	0.138
Earth Shield to Radiator Backload Radiation	0.188
Solar Scatter Earth Shield to Radiator Radiation	0.093
Total	1.758 W
Resultant Radiator Temperature = 163K	
Conductance Element	Gradient (K)
Heat Transfer Rod	1.3
Thermal Strap	8.9
Total for Interfaces	2.0
Total CFP to Radiator Gradient	12K
Resultant Cold Focal Plane Temperature = 175K	

Thermal control of the instrument is predicated upon isolation from the payload mounting plate with a conductance of less than 0.01 W $inch^{-2}$ (as per the spacecraft requirement) and use of a 200 cm^2 area of the outboard exterior of the electronics module painted white with a space view exposure to serve as a thermal control radiator. Power dissipation variation throughout the

orbit is minimized by use of a replacement heater when the scan assembly is not powered. All exterior surfaces except for the thermal control radiator, CFP radiative cooler, earth shield, and rotating aperture/sunshield will be covered with multi-layer thermal blankets. Blankets identical to those designed for the low earth orbiting Landsat series sensors are proposed for EOSP. These blankets use ten dacron layers, each 0.00025 inch thick, for separating the ten super insulation layers of 0.00025 inch thick aluminized kapton. The outer layer is 0.002 inch thick kapton with the aluminized side facing out. A preliminary thermal analysis (CINDA model) indicates thatfor the specified PMP extreme temperatures of +60°C and -25°C, the corresponding EOSP instrument temperatures are +35°C and +7°C, respectively.

Physical Properties. The overall envelope of the EOSP excluding the solar diffuser assembly and with the earth shield in the stowed launch position is 50.8 cm in the platform track direction (x-axis), 26.0 cm in the cross-track direction (y-axis), and 37.5 cm in the nadir direction (z-axis) as illustrated in Figure 19. Deployment of the earth shield adds 5.7 cm to the height (z-axis) and 30.5 cm to the outboard y-axis envelope. The solar diffuser assembly adds 31.6 cm in height with the diffuser in the stowed position and adds 53.6 cm in the deployed position. Final values for these latter two dimensions will be dependent of spacecraft accomodation requirements.

The EOSP total instrument mass of 16.2 kg is distributed among the major subassemblies and mechanisms as indicated in Table 5. The mass moments of inertia with respect to the instrument center of mass are 2122 kg cm^2 about the x-axis, 3866 kg cm^2 about the y-axis, and 3231 kg cm^2 about the z-axis.

Assembly Process. The modular nature of the EOSP design allows for an assembly process which maximizes the simultaneous parallel activities of assembly. The halfwave retarder wheel will be completed and attached to the motor/encoder. This assembly is then installed into the octagonal structure. Assembly operations involving the twin scan mirror assembly and the eight telescopes can be done in parallel. Verification of alignment for each telescope can be accomlished by using special test equipment which represents both the scan mirror set and the CFP. Final adjustments of alignments will be made at the full assembly level.

Vacuum sealing windows must be bonded to the octagonal structure. The skeleton structure can be assembled upon receipt of the bulkheads, baseplate, and octagonal structure. Next, the retarder assembly is loaded into its seat inside the octagonal structure. As they become available from optics, the eight telescopes are positioned against their registration surfaces. The adjustment clearance between adjoining telescopes is 1 mm and there is a similar clearance near the

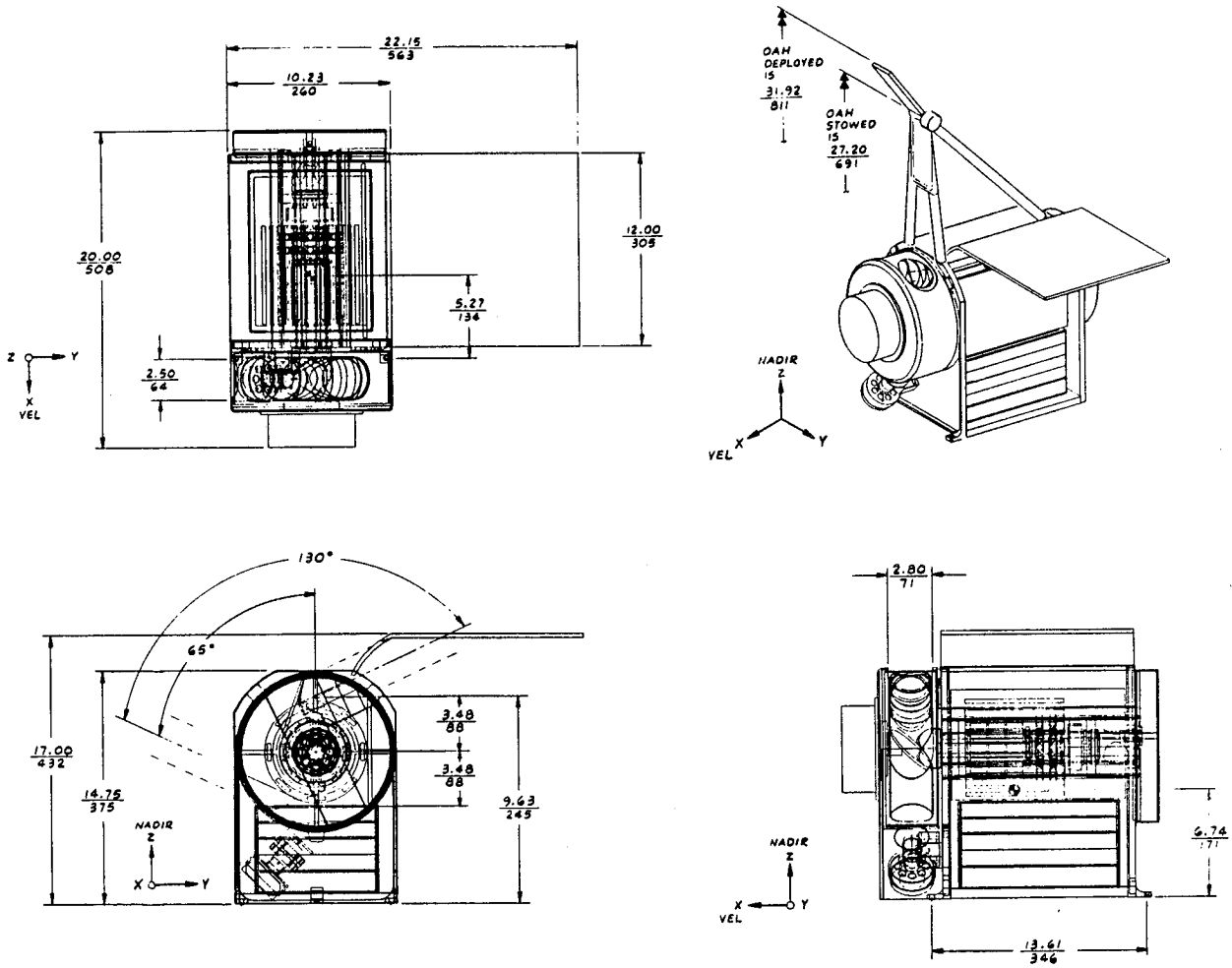

Figure 19. EOSP instrument outline.

Table 5. EOSP Mass Breakdown by Assembly

Assembly	Mass (kg)
Scan drive assembly	2.52
Telescope assemblies	1.40
Telescope mount assembly	2.76
VINIR detectors and preamps	0.41
CFP assembly, preamps, and radiative cooler	0.73
Retarder motor assembly	0.33
Polarization calibrator assembly	0.39
Electronics modules	5.02
Thermal control elements	0.94
Solar diffuser assembly	0.30
Latch assemblies	0.26
Miscellaneous (including cables)	1.10
Total mass	16.2 kg

retarder wheel. The scan drive assembly and electronics modules can be installed as they pass their consent to integrate reviews.

The long-duration work on the four cold focal plane modules can progress in parallel with the electro-optical-mechanical work. Detector elements are screened and then bonded to the substrates. The field lenses are bonded over the detectors. Fine line cables are restrained and wire-bonded to the substrate traces. Each module must undergo functional testing at temperature prior to attachment to the flight cold stem. Select components will be identified with test equipment and this information used by electronics to build the preamplifier boards. Focal plane alignment of the modules to the stem is performed during assembly. Initial top level adjustment is provided by moving the CFP relative to the octagonal structure. Final drilling/pinning of the CFP assembly will be done after initial optical testing. Final adjustment to the detectors is achieved by parallel translations of the telescope assemblies in the y- and z-directions.

The assembly and testing of the electronics can proceed independently of the opto-mechanical assembly, including build-up of the electronics modules (component installation and mounting of the connectors and boards into the structural frames). The integrated electronics module can be fitted to the top assembly at any convenient time with minimal disturbance to other subassemblies.

Contamination Control. In addition to the special contamination controls employed during optical assembly and during the opto-mechanical-electronic integration, the selection of materials for the non-optical subassemblies within the instrument shall be made with emphasis on choices which reduce overall contamination within the instrument. In general, materials selected for use internal to the instrument shall have a total mass loss (TML) of less than 1 percent and a collected volatile condensable mass (CVCM) amount of less than 0.1 percent. Where functionally equivalent materials are available, the one with the lowest TML and CVCM will be selected. All lower level components will be inspected and cleaned prior to assembly. Aluminum surfaces will be rigorously cleaned and coated (e.g., chromate conversion coating) to guard against oxidation. All velcro hook and pile strips will be thoroughly vacuum baked before being used in multi-layer thermal blanket construction, and all thermal blankets will be vacuum baked after receipt from the vendor.

2.6 ELECTRONICS

Overview of Electronics. An electronics design compatible with EOS spacecraft interfaces can be developed for the EOSP with present technology while drawing heavily from the designs of polarimeter instruments built for the Pioneer and Galileo missions. The EOSP instrument will

be designed using many components and subassemblies from those designs which have demonstrated the feasibility of unserviced operation for as long as 15 years.

Figure 20 shows the functional electronics block diagram for the EOSP. The analog electronics will process the outputs from the 32 silicon (VINIR) and 16 HgCdTe (SWIR) detectors including the amplification, bandpass filtering, and analog multiplexing. Digital signal processing will provide the 14-bit sample quantization, format the digital outputs, insert engineering data and transmit the bit stream to the EOS spacecraft interface, and control the system actuators, heaters, and calibration lamps.

Analog Signal Processing. As illustrated in Figure 21, both detector types will use differential transimpedance preamplifiers mechanized with FET-input operational amplifiers with feedback resistors of 50 Mohm (VINIR) and 30 Mohm (SWIR). The cooled (HgCdTe) focal plane preamplifiers will have an additional first stage FET pair and the feedback resistors mounted near the detectors on the radiative cooler cold stage. These will be packaged as four independent quadrant subassemblies, each interfaced to the ambient temperature electronics with four identical low thermal conductivity flat cables similar to the ones used for the Landsat Thematic Mapper instrument. Noise contribution from both preamplifiers will be dominated by feedback resistor noise over the 166 Hz signal bandwidth. The boosted preamplifier voltage noise is not significant because the amplifier summing junction capacitance for both preamplifier types will be less than 15 pf, making the noise boost corner frequency above the upper band limit. Preamplifier current noise (for either type) is not significant if FET gate leakages remain below about 50 pA. Radiation testing of both types will ensure that the noise performance does not degrade with lifetime.

After preamplification, the analog circuitry for both detector types will be identical (cf. Figure 21) and consist of: (1) a ground commandable x2 or x4 gain stage to scale the detector signals to 0.5V and drive the dc restore coupling capacitor; (2) a second (high input impedance) gain stage to amplify the signals to approximately 2.5V; (3) a resetting integrator low-pass filter; (4) a dc restore feedback amplifier and FET switch; and (5) a unity gain sample and hold to sample the integrated signal value for digitization.

The dc-restore loop (similar to that used on the Galileo PPR instrument) will remove channel offsets and 1/f noise drift once each mirror scan while the detectors view a dark reference surface within the scan mirror assembly housing. During the restore interval, the integrator "reset" switch is turned on, converting the integrator to a x1 inverting amplifier. The output is compared to a reference voltage (the desired channel operating output voltage) and the difference is applied to the channel coupling (dc restore) capacitor via the restore switch, causing the

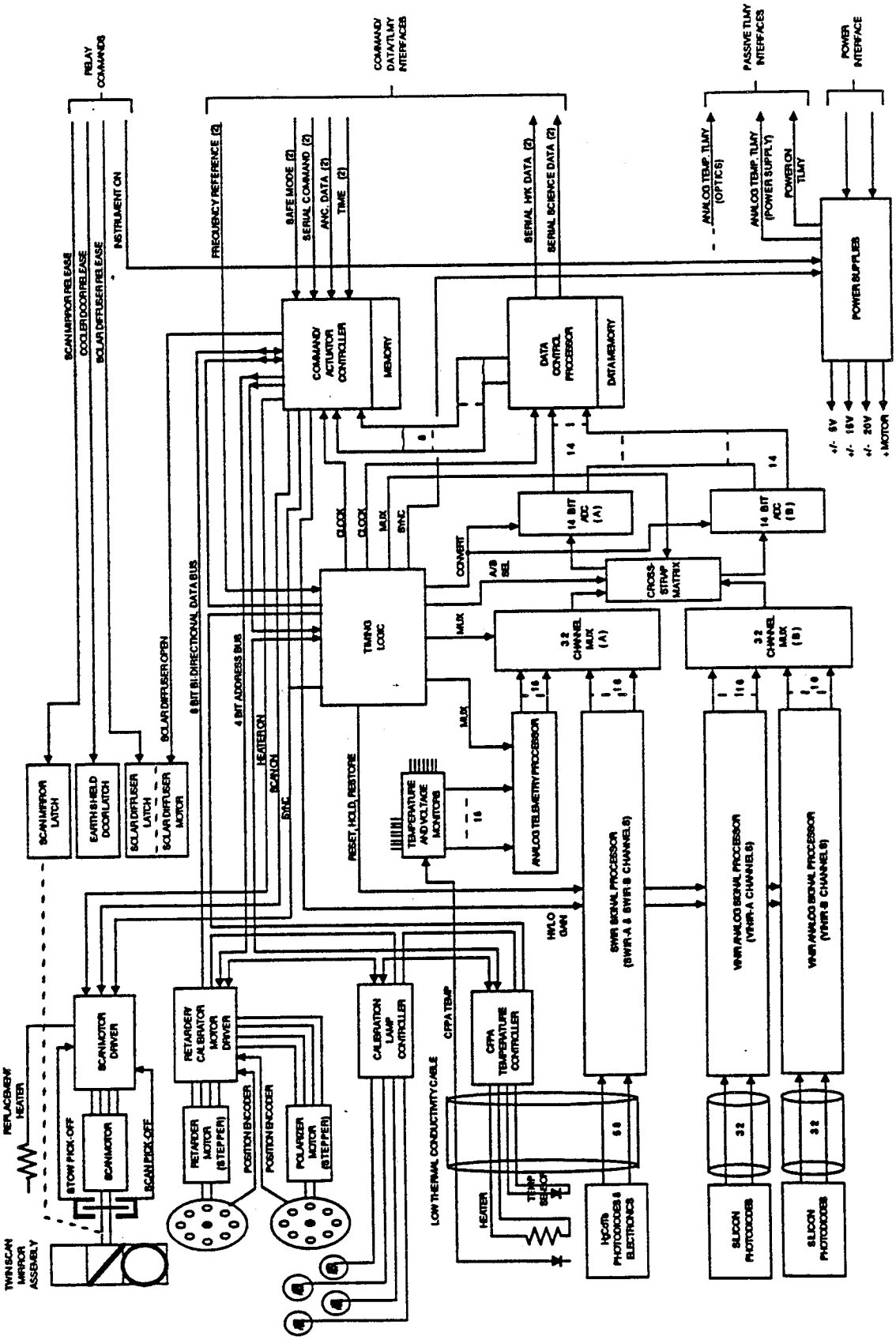

Figure 20. EOSP electronics functional block diagram.

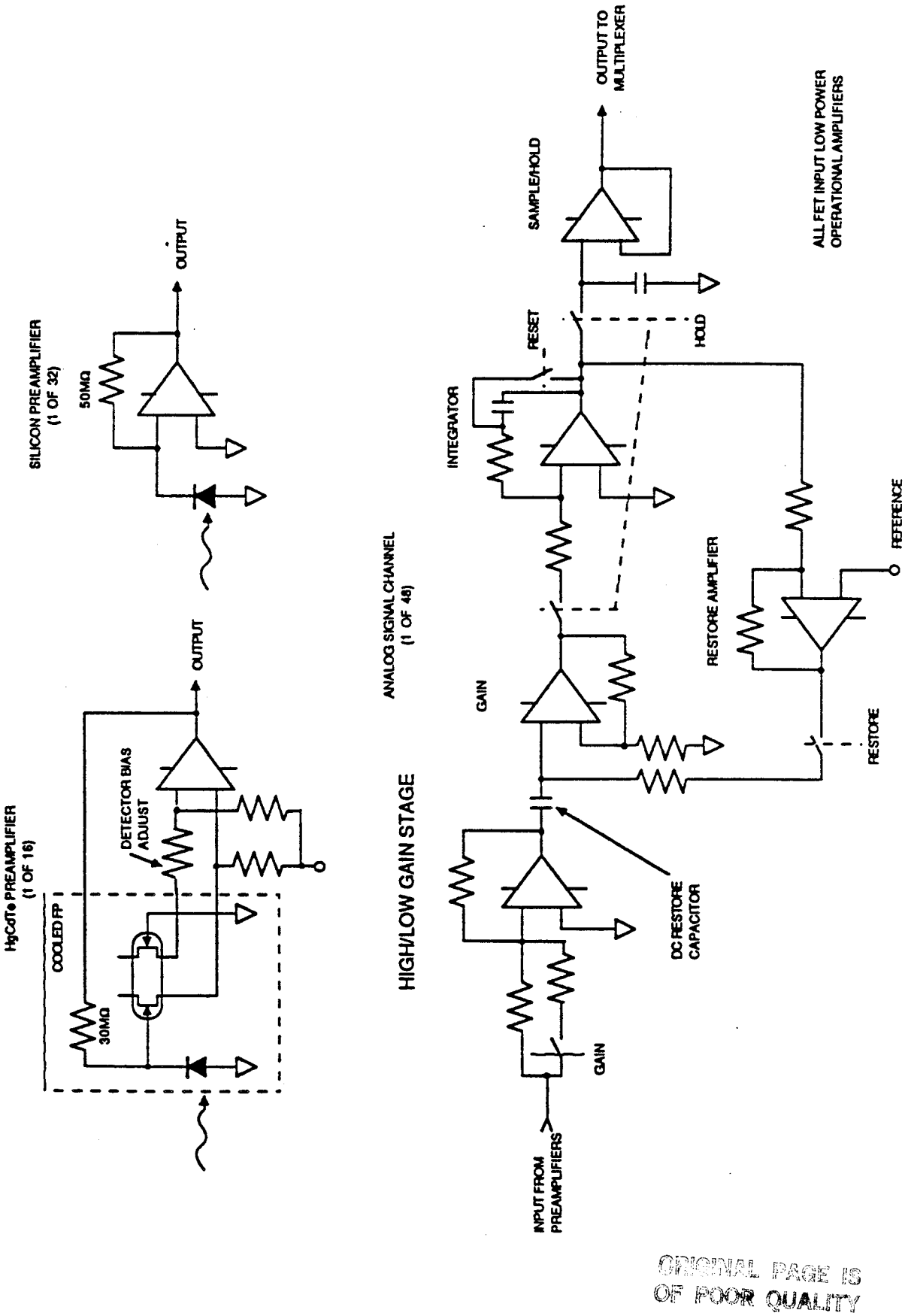

Figure 21. Analog signal processor.

channel output to servo to the restore reference level. After restoration, the restore switch is opened and the channel bias holds because the amplifier following the restore capacitor has an extremely high input impedance and therefore removes no charge during the next mirror scan.

Resetting integrators are the preferred type of low-pass filtering because they have no inter-sample memory and they are easily mechanized having no select components. The hold circuit "acquire" and integrator "reset" will be performed in less than 100 μs of the 3.3 ms integration period, so that only 3% of the scene viewing time will be lost for each data sample.

Channel outputs will interface with 32 channel multiplexers and dual Micro-Networks MN5284 analog to digital converters (ADCs). Both multiplexer outputs will be capable of addressing either ADC through cross-strapping switches to provide partial instrument operation in case of an ADC failure. The cross-strapping switches will be programmable via the instrument serial command to provide 16 different data formats without changing the instrument to spacecraft data format. Only the 14 high-order bits of the 16 ADC bits will be put into the instrument data stream. Radiation testing will be performed to determine whether shielding of the ADCs is required to retain sufficient accuracy. The Galileo PPR instrument required localized shielding for the ADC.

Digital Electronics. Dual Harris 80C86 microprocessors will be used as system controllers. Harris (radiation hard) processors are presently being used for Mars Observer and are latch-up free and total dose tolerant to 10^6 rads. Local radiation shielding will be provided in the instrument design to ensure that single event upsets do not interfere with normal operation. The first microprocessor will decode BDU commands and interface with the instrument actuator control electronics over a bi-directional data bus. Operation of the stepper motor servo loops and the lamp and heater controllers via the microprocessor allows power load sharing so that coincident power peaks are avoided. This processor will also interface (via the same bus) with hard-wired CMOS logic which will provide the realtime signals required to control the analog channels and synchronize the power supply and scan mirror. The second microprocessor will format instrument outputs for the housekeeping (BDU) serial data bus and instrument science data (1553B) bus. The science data will be transferred to the redundant busses by an interface controller such as the 65112 by DDC, which provides redundant decoding and driving circuitry. Data storage requirements for a single, 1.48-sec scan are small, viz., only 16Kbytes, so spare memory sections will be provided and tested by the processor at power turn-on.

Power Electronics. Operating voltages for the instrument electronics will be converted from the 120 Vdc spacecraft power bus by a transformer isolated (synchronized) pulse width modulated switching inverter. Soft-start circuitry will minimize turn-on transients and prevent

stressing of the instrument fuse located on the payload mounting plate. Low shunt capacitance input filters will ensure that bus-feedback ripple meets the spacecraft requirements. A separate transformer will be provided for pulsed power loads (such as the stepper motors) to provide transient isolation for the analog circuitry. Low headroom series regulators will be used for all instrument voltages.

Power drivers for the scan motor, retarder and calibrator motors, calibration lamps, cold focal plane heater, and solar diffuser thermal actuator will be controlled using a bi-directional data bus. The cold focal plane heater will be restricted to 150 mW (maximum), and eight different ground commandable temperature control points will be provided in case the radiative cooler becomes contaminated over many years of service. This approach is feasible because the detector responsivity and overall system noise are only weak functions of temperature. The remaining power drivers will be similar to those used successfully on previous instruments. Power dissipation by assembly is given in Table 6.

Table 6. EOSP Power Dissipation by Assembly

Assembly	Average Power (Watts)	Pulsed Power (Watts, Maximum)
Power Supply Module	2.95	
Digital Electronics Module	1.60	
Multiplexer/ADC Module	0.95	
Analog Module #1	0.90	
Analog Module #2	0.90	
VINIR (Silicon) Preamplifiers	0.20	
SWIR (HgCdTe) Preamplifiers	0.15	
Scan Motor/Replacement Heater	4.50	
Calibration Lamps	0.02	2.50
Cold Focal Plane Heater	0.10	0.20
Calibrator/Retarder Motors	0.01	4.50
BDU (approx. 10% duty cycle)	1.75	4.00
Total	14.0	(See Text)

Note that the commandable pulsed power loads are never coincident. For example, the calibration lamps will not be operated while the retarder motor is being stepped, and the power to the solar diffuser will be cycled "off" when the calibration lamps are on. The timing of the BDU power peaks is not controlled and may thus occur simultaneously with other peaks, leading to a possible peak power of 22.5 W.

2.7 INSTRUMENT TEST AND CALIBRATION

Summarized in Table 7 are key performance requirements that are verified during: (1) electronic board assembly, electronic module integration, and electronics/optics integration; (2) bench testing that includes complete functional checkout of the instrument, characterization of key optical parameters, and radiometric and polarimetric calibration; and (3) thermal vacuum testing where both functionality and instrument calibration characterizations as a function of temperature are performed. The recommended sequence of instrument acceptance and calibration testing that begins upon completion of the assembly of the instrument is indicated in Figure 22. Further compatability verification (and perhaps instrument-to-instrument calibration comparisons) will be performed as a part of payload mounting plate/spacecraft integration and test programs. Successful completion of this test program will provide the desired confidence that the EOSP is flight ready.

An example of the planned pre-flight testing is the radiometric calibration of the EOSP instrument. One type of measurement set will consist of viewing a diffuse reflectance target of pressed Halon fabricated by a well-controlled process to produce a target of known bidirectional reflectance distribution function (BRDF). The target is illuminated at normal incidence and fixed source-to-target distance by a halogen-cycle, tungsten filament lamp with the spectral irradiance calibration traceable to NIST. This combination serves as a suitable spectral radiance standard. Measurements when viewing this source plus measurments of the relative spectral response of the EOSP spectral bands allow proper transfer of the spectral radiance of the standard to the weighting that would result when a solar distribution is viewed. Such measurements allow a proper calibration the radiance responsivity of the 48 EOSP channels with the implicit assumption that the scene reflectance is essentially constant across each EOSP spectral band.

Table 7. Summary of EOSP Pre-delivery Performance Requirement Verifications

	Assembly Test				Unit Test	System Integ./Accept. Test		
Performance Requirement	Power Supply	Comd. Proc.	Analog/ Dig. Con.	Analog Proc.	Elec. Integ.	Optics Integ.	Bench Test	Thermal Vac Test
Gnd Isolation	•	•	•	•	•	•		
Gnd Continuity	•	•	•	•	•	•		
Power Use	•	•	•	•	•	•	•	•
Vin Transients	•							
Vin Range	•					•	•	•
Command Oper.		•			•	•	•	•
Retarder Whl Pos		•			•	•	•	•
Motor Controls		•			•	•	•	•
Heater Controls	•	•			•	•	•	•
Gain Control		•	•	•	•	•	•	•
A/D			•		•	•	•	•
Linearity			•		•	•	•	•
SNR						•	•	•
Elec. Crosstalk			•	•	•	•		
Gain			•	•		•	•	•
Offset			•	•		•	•	•
Bandwidth			•					
Tlmy Circuits			•		•	•	•	•
Temp Test	•	•	•	•	•			•
IFOV Alignment						•		
MTF Matching						•	•	•
Opt. Axis Align.						•	•	
Scat. Light Resp.							•	
Rel. Spect. Resp.							*F	
Intg. Out-of-Band							•	•
Polarimetric Calib.						•	•	•
Radiometric Calib.							•	•
Vibration							•	
Shock							D	
EMC							D	
Magnetic Sign.							D	

D = Tests performed at Spacecraft Integration
F = Based on piece part filter measurements

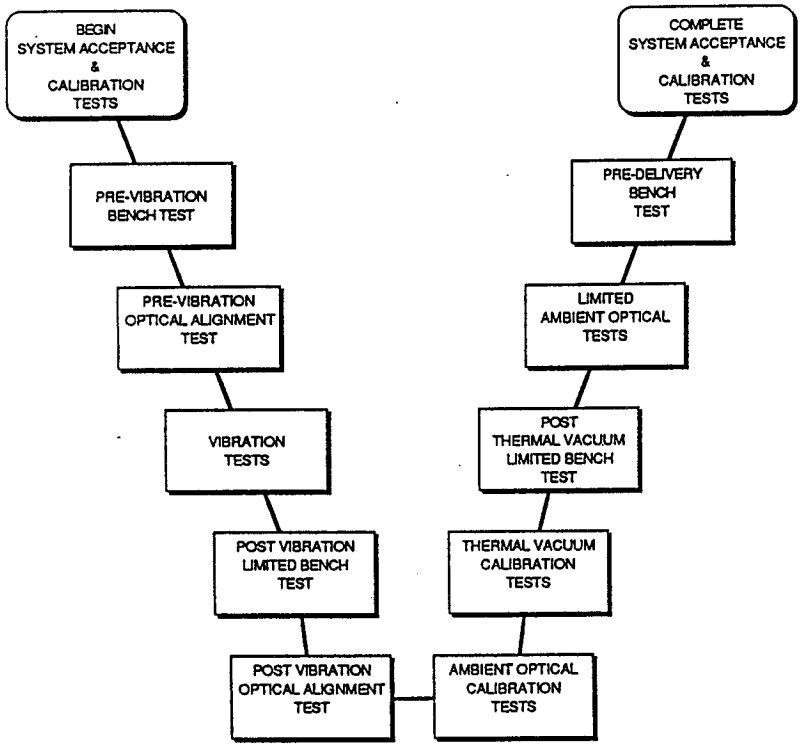

Figure 22. EOSP system test and calibration plan sequence.